

SPICE Connection Mosaics to link the Sun's surface and the heliosphere

T. Varesano^{1,2}, D. M. Hassler¹, N. Zambrana Prado³, J. Plowman¹, G. Del Zanna¹⁵, S. Parenti⁵, H. E. Mason¹⁵, A. Giunta⁴, F. Auchère⁵, M. Carlsson⁶, A. Fludra⁴, H. Peter⁷, D. Müller⁸, D. Williams⁹, R. Aznar Cuadrado⁷, K. Barczynski¹⁰, E. Buchlin⁵, M. Caldwell⁴, T. Fredvik⁶, T. Grundy⁴, S. Guest⁴, L. Harra¹¹, M. Janvier⁵, T. Kucera³, S. Leeks⁴, W. Schmutz¹⁰, U. Schuehle⁷, S. Sidher⁴, L. Teriaca⁷, W. Thompson¹⁴, and S. L. Yardley^{12,13}

¹ Southwest Research Institute, Boulder, CO 80302, USA

² Institut National Polytechnique de Grenoble, 38000 Grenoble, France

³ NASA Goddard Space Flight Center, Greenbelt, MD, USA

⁴ RAL Space, UKRI STFC Rutherford Appleton Laboratory, Didcot, United Kingdom

⁵ Université Paris-Saclay, CNRS, Institut d'Astrophysique Spatiale, 91405, Orsay, France

⁶ Institute of Theoretical Astrophysics, University of Oslo, Norway

⁷ Max-Planck-Institut für Sonnensystemforschung, Göttingen, Germany

⁸ European Space Agency, ESTEC, Noordwijk, The Netherlands

⁹ European Space Agency, ESAC, Villanueva de la Canada, Spain

¹⁰ Physikalisch-Meteorologisches Observatorium Davos, World Radiation Center, Davos Dorf, Switzerland

¹¹ ETH Zürich, IPA, Hönggerberg campus, HIT J22.4, Wolfgang-Pauli-Str. 27, 8093 Zürich

¹² Department of Meteorology, University of Reading, Earley Gate, Reading, RG6 6BB, UK

¹³ Donostia International Physics Center (DIPC), Paseo Manuel de Lardizabal 4, San Sebastián, 20018, Spain

¹⁴ ADNET Systems, Inc., Lanham MD, USA

¹⁵ DAMTP, Centre for Mathematical Sciences, Wilberforce Road, Cambridge CB3 0WA, UK

Received XXX; accepted XXX

ABSTRACT

Aims. We present an analysis of the first connection mosaic made by the SPICE instrument on board of the ESA / NASA Solar Orbiter mission on March 2nd, 2022. The data will be used to map coronal composition that will be compared with *in-situ* measurements taken by SWA/HIS to establish the coronal origin of the solar wind plasma observed at Solar Orbiter. The SPICE spectral lines were chosen to have varying sensitivity to the First Ionization Potential (FIP) effect, and therefore the radiances of the spectral lines will vary significantly depending on whether the elemental composition is coronal or photospheric.

Methods. We perform temperature diagnostics using line ratios and Emission Measure (EM) loci, and compute relative FIP biases using three different approaches (two line ratio (2LR), ratios of linear combinations of spectral lines (LCR), and differential emission measure (DEM) inversion) in order to perform composition diagnostics in the corona. We then compare the SPICE composition analysis and EUV data of the potential solar wind sources regions to the SWA / HIS data products.

Results. Radiances maps are extracted from SPICE spectral data cubes, with values matching previous observations. We find isothermal plasma of around $\text{Log}T = 5.8$ for the active region loops targeted, and that higher FIP-bias values are present at the footpoints of the coronal loops associated with two active regions.

Key words. Techniques: spectroscopic — Sun: Abundances — Sun: Transition region — Sun: Corona — Sun: UV Radiation

1. Introduction and motivation

The heliosphere is a low-density medium composed mainly of plasma, radiation, dust, and energetic particles. Characterizing this medium has been a long-standing goal in the field, with the aim of relating its properties to the magnetic activity of the Sun, as well as having a better understanding of the effects experienced by the various bodies immersed in this highly dynamic medium. The flows which generate the solar wind drive the evolution of the heliospheric magnetic field, and are therefore a prime source of information to answer the questions we are addressing in this paper. The *Solar Orbiter* (Solo) mission (Müller et al. 2013, 2020; García Marirrodriga et al. 2021) with its six remote sensing and four *in-situ* instruments provides a comprehensive diagnosis of solar plasma as well as solar wind plasma, providing insights into the origin of solar winds and the factors

responsible for the generation and acceleration of the solar wind to speeds of hundreds of kilometers per second. Solar Orbiter will substantially build on the observations of the Helios mission (Winkler 1976), taking the closest ever images of the Sun and directly observing the high latitude polar regions for the first time with its out of the ecliptic orbit.

As part of Solo's remote sensing suite, the SPectral Imaging of the Coronal Environment (SPICE) instrument (SPICE Consortium et al. 2020; Fludra et al. 2021) is an imaging spectrometer that records extreme ultra-violet (EUV) spectra of the Sun. SPICE provides a complete temperature coverage, from the low chromosphere to the high corona, as well as powerful off-limb coronal diagnostics. SPICE will produce Doppler velocity maps (e.g. Hassler et al. (1999)) as well as detailed composition diag-

nostics, thanks to its various simultaneously observable emission lines from low and high First Ionization Potential (FIP) elements.

One of the strengths of the instrument is its ability to compare its data products with those from *in-situ* instruments such as the Solar Wind Analyser's Heavy Ion Sensor (SWA-HIS; Owen et al. 2020b). By linking remote sensing observations of the solar corona and transition region with *in-situ* measurements of plasmas, fields, and energetic particles, it is possible to understand how solar processes are related to the plasma phenomena in the heliosphere and how the heliosphere is generated.

Even though the origins of the fast solar wind are well known (Krieger et al. 1973; Cranmer et al. 2007), there are still open questions regarding the formation and mechanisms of the slow solar wind (Abbo et al. 2016; Cranmer et al. 2017; Borovsky 2020). SPICE's mosaic data will aid in explaining the formation of the slow solar wind, particularly by studying the FIP effect – the enhancement of low-FIP elements in the corona (Parenti et al. 2021), which has been a topic of intense investigation in recent years.

In this paper, we present an analysis of the first composition mosaic from SPICE, and we demonstrate a variety of the possibilities for future remote sensing observations of this nature. In Section 2, a description of the data and observations is provided, and we present and analyze the results in Section 3. Section 4 describes FIP-bias measurement techniques and results. In Section 5, we discuss problems with the data, avenues of improvement, and future plans. We perform a partial replication of the analysis conducted in Brooks et al. (2022) on November 2020 data (e.g. intensity diagnostics, EM loci analysis and Mg/Ne measurements) and extend it by performing additional diagnostics on SPICE's new measurements, such as abundance and temperature diagnostics. In this paper, we seek to continue to build on previous work carried out on establishing new methodologies for interpreting measurements from SPICE.

2. Data and observations

SPICE operates in two modes: using a fixed slit position (*sit-and-stare*); or by scanning the Sun in the direction perpendicular to the slit (*rastering*) (SPICE Consortium et al. 2020; Fludra et al. 2021). It has four available slits of varying widths (2'', 4'', 6'', and 30'').

Two wavelength ranges are observed with SPICE: 704 to 790 Å with the SW (short wavelength) detector, and 973 to 1049 Å with the LW (long wavelength) detector. The spectral lines observable in both these ranges are produced by a number of different ions. These ions allow for the investigation of the relationships between all the observed layers of the solar atmosphere since they form at temperatures from 10 000 K (observable with SPICE's H I) to 10 MK, reached by Fe XX (Table 1 of SPICE Consortium et al. (2020)).

On March 2nd 2022, SPICE performed three raster observations as part of the first occurrence of the Composition Mosaic SOOP (Solar Orbiter Observing Plans, Zouganelis et al. (2020)), which included all ten instruments: six remote sensing ones - SPICE, the Extreme UV Imager (EUI; Rochus et al. (2020)), the Polarimetric and Helioseismic Imager (PHI; Solanki et al. (2020)), the Spectrometer Telescope for Imaging X-rays (STIX; Krucker et al. (2020)), Visible light and UV Coronagraph (Metis; Antonucci et al. (2020)) and the Heliospheric Imager (SoloHi; Howard et al. (2020)), and four *in-situ* ones: Solar Wind Analyser (SWA; Owen et al. (2020a)), Radio and Plasma Wave analyser (RPW; Maksimovic et al. (2020)), Magnetometer

(MAG; Horbury et al. (2020)), Energetic Particle Detector (EPD; Rodríguez-Pacheco et al. (2020)).

The composition mosaic observations lasted from 00:41 to 23:30 UTC while Solar Orbiter was very close to its first perihelion, at around a heliocentric distance of 0.54 AU.

SPICE has a spatial resolution along the slit of about 4'' and a spectral resolution of 0.09 Å. For this study, each recorded raster contains the same seven spectral intervals, or spectral windows, with an exposure time of 120 seconds. These spectral windows have been chosen to provide a uniform distribution of formation temperatures for the spectral lines, to sample multiple ions in each temperature range, and to provide the largest possible discrimination in FIP. Each window has a different spectral size, and in some of them a few spectral lines are blended. These blends require particular attention when computing the radiances of the spectral lines. A method to separate these blended lines will be presented in this section.

The SPICE data pipeline provides calibrated data, the spectra have been corrected for slit tilts, detector misalignments and other distortions as well as flat-field and dark current (SPICE Consortium et al. 2020). Currently, the pipeline does not account for the decline of the instrument's responsivity since the beginning of the mission. This decline is happening uniformly across the SW and LW wavelength bands, affecting all lines equally. Consequently, the signal levels for a specific date close to the launch (2020) will differ from those in March 2022. We expect the disparity between November 2020 and March 2022 to be approximately of a 2.5 factor. The burn-in (the degradation of the detectors due to long exposure to high intensities) is also to be taken into account, affecting mainly the N IV and Ne VIII lines, and to a lesser extent the N III and O III lines. Quantifying the burn-in factor of the last two lines poses a greater challenge due to the complexity of the region and the camera artifacts.

While looking at the rasters, horizontal-line noise prevented the data from being correctly processed. We partly addressed this issue by subtracting, from each y - λ plane, the plane's minimum value; this removed some horizontal banding artifacts. We also binned down the rasters by a factor of two along the X axis in order to improve computation times and signal-to-noise ratios.

2.1. Solar features observed in the mosaic

During this first SOOP Mosaic, two active regions (ARs) were in SPICE's Field of View (FOV). NOAA 12958, on the "A" panel of the radiance maps depicted in Fig. 2, was caught during the first raster scan, and NOAA 12957 lies in between panel "B" and "C". These reported ARs were identified using the NOAA Active Region (NAR) database and the Solar Monitor software (Gallagher et al. 2002), and an extensive study on decayless kink oscillations by Berghmans et al. (2023) using EUI data has been conducted on those two ARs. Both ARs are simple bipoles, with a distinct separation between the positive and negative polarities, and hence are classified as β regions. Their characteristics are summarized in Table 2.

The simple nature of the bipoles is clearly evident in the photospheric magnetic field data, in the top panel of Figure 1. We show the line-of-sight magnetogram taken by SDO/HMI on March 2nd 2022 at 18:58 UT. From the magnetograms it is evident that AR 12958 is a decaying field region whereas, AR 12957 consists of multiple emerging structures. On AR 12957, two major bipoles can clearly be identified on the top panel of Figure 1 (b) and related to the loops that can be seen on the bottom panel of Figure 1 (b). Negative polarities (denoted in black) on the

Spectral lines	logT (K)	FIP (eV)	Transition	Sub-windows (Å)	Spectral bin
O I 988.6	4.2	13.6	$2s^2 2p^4 \ ^3P_2 - 2s^2 2p^3 \ ^2D_0$	987.4 – 989.1	(1,1)
N III 989	4.8	14.5	$2s^2 2p^2 \ ^1P_{1/2} - 2s 2p^2 \ ^2D_{3/2}$	989.1 – 990.6	(1,1)
N III 991 *	4.8	14.5	$2s^2 2p^2 \ ^3P_{3/2} - 2s 2p^2 \ ^2D_{3/2}$	990.6 – 993.4	(1,1)
O III 702.8 *	4.9	13.6	$2s^2 2p^2 \ ^3P_1 - 2s 2p^3 \ ^3P_0$	700.3 – 703.1	(1,1)
O III 703.8	4.9	13.6	$2s^2 2p^2 \ ^3P_2 - 2s 2p^3 \ ^3P_1$	703.1 – 704.85	(1,1)
S IV 748	5.0	10.4	$3s^2 3p \ ^2P_{1/2} - 3s 3p^2 \ ^2P_{1/2}$	746.1 – 749.0	(1,1)
S IV 750	5.0	10.4	$3s^2 3p \ ^2P_{3/2} - 3s 3p^2 \ ^2P_{3/2}$	749.0 – 752.3	(1,1)
N IV 765₁ *	5.1	14.5	$2s^2 \ ^1S_0 - 2s 2p \ ^1P_1$	762.37 – 767.15	(2,1)
S V 786 *	5.2	10.4	$3s^2 \ ^1S_0 - 3s 3p \ ^1P_1$	784.2 – 787.0	(1,1)
O IV 787 *	5.2	13.6	$2s^2 2p \ ^2P_{1/2} - 2s 2p^2 \ ^2D_{3/2}$	787.0 – 789.8	(1,1)
O VI 1032 * ₁	5.4	13.6	$1s^2 2s \ ^2S_{1/2} - 1s^2 2p \ ^2P_{3/2}$	1029.14 – 1034.91	(2,1)
Ne VIII 770 *	5.8	21.6	$1s^2 2s \ ^2S_{1/2} - 1s^2 2p \ ^2P_{3/2}$	767.2 – 771.5	(2,1)
Mg VIII 772	5.9	7.6	$2s^2 2p \ ^2P_{3/2} - 2s 2p^2 \ ^4P_{5/2}$	771.5 – 775.2	(2,1)
Mg IX 706 *	6.0	7.6	$2s^2 \ ^1S_0 - 2s 2p \ ^3P_1$	704.85 – 708.1	(1,1)

Table 1: Lines extracted from the mosaic data set, and the wavelength window used to determine the Gaussian parameters for the fitting. In bold are the four lines we use for the LCR relative FIP bias measurements. Lines marked with ‘*’ were used to infer the DEM. Lines with an index ₁ indicate those which only require a single Gaussian fit, therefore the ones that should give the best results. Windows marked with a bin of (2,1) were binned in the spectral direction by a factor of two on-board, the rest were not.

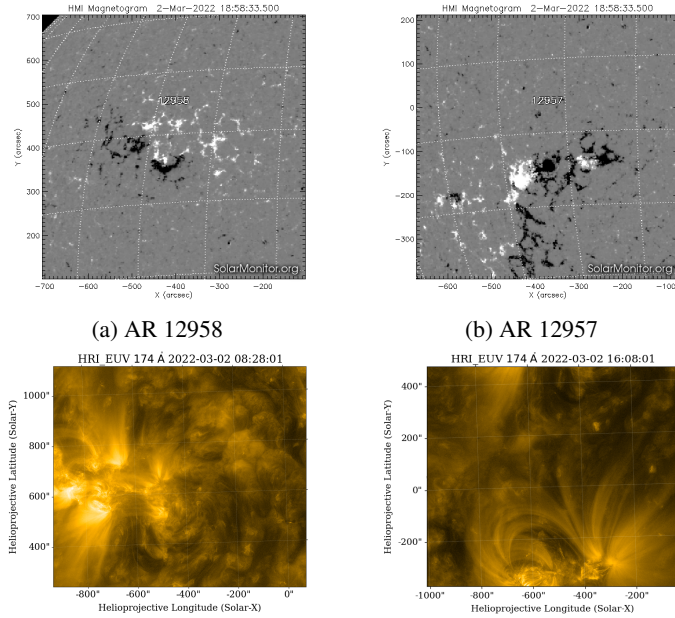


Fig. 1: Active Regions 12958 (a) and 12957 (b) observed on March 2nd, 2022 by EUV/HRI imager at 174 Å (representing the corona at 0.9 MK) and corresponding SDO/HMI images observed on March 2nd, 2022 at 18:58 UT. White/black areas are of positive/negative polarity. The field of view of the two instruments are slightly different due to different pointing between SPICE and HRI (refer to coordinates on the axes).

HMI images are also spatially consistent with the loops at the edges of the active region, which could be associated with open magnetic field.

2.2. Spectral line fitting

Once the SPICE pre-processing has been applied, a Gaussian fit of the emission peaks is performed. Two cases can be encountered, namely single or multiple line fitting. When a line has a narrow spectral size (typically under 25 pixels) and a single ion

Parameter	NOAA 12958	NOAA 12957
Concept	Active Region	Active Region
Hale class	β	β
McIntosh class	Cro	Cro
Solar X	-390''	-356''
Solar Y	403''	-89''
Sunspot area	20	30 (millionths)
Number of spots	2	5
Associated flares	M2.0(17:31)	-

Table 2: Technical description of observed ARs.

of interest is present, a single Gaussian is fitted onto the spectrum. If the window is wider but only one line is worth observing, a windowing of the spectrum is applied to define a particular region for the fitting. In the second case, several ions of interest are blended within a single window; we then fit the spectra with a model including several Gaussians. Regardless of the case, the continuum is modeled by a constant.

More details about the line fitting method and the windows are given in Appendix A, and the main characteristics of the lines are shown in Table 1. Examples of the radiances derived from the fitting and their distribution are presented in Figure 2, and the complete radiance diagnostic containing all of the extracted lines is shown in Appendix C. The chromospheric network can be clearly identified at lower temperatures (0.06-0.3 MK), and brighter, hotter loops start to be visible around 0.3 MK, (e.g. O VI 1032) line. All the lines show very bright moss – low-lying, reticulated EUV emission and the base of hot and high-pressure loops, discovered in *TRACE EUV Fe IX/X* images (Berger et al. 1999) – emission at the footpoints of the loops. Noticeably darker pixels represent unsuccessful fitting, mainly due to noisy spectra.

In order to validate the results of the line fitting, we compare our values with previous SPICE measurements from Brooks et al. (2022) and the compilation of quiet Sun radiances, mostly from SUMER, listed by Dufresne et al. (2023). To compare the values of the area *SI* observed in Brooks et al. (2022) (AR 12781), we took two similar active regions, denoted S1 and S4 on Figure 3. SUMER values are computed over a quiet Sun area;

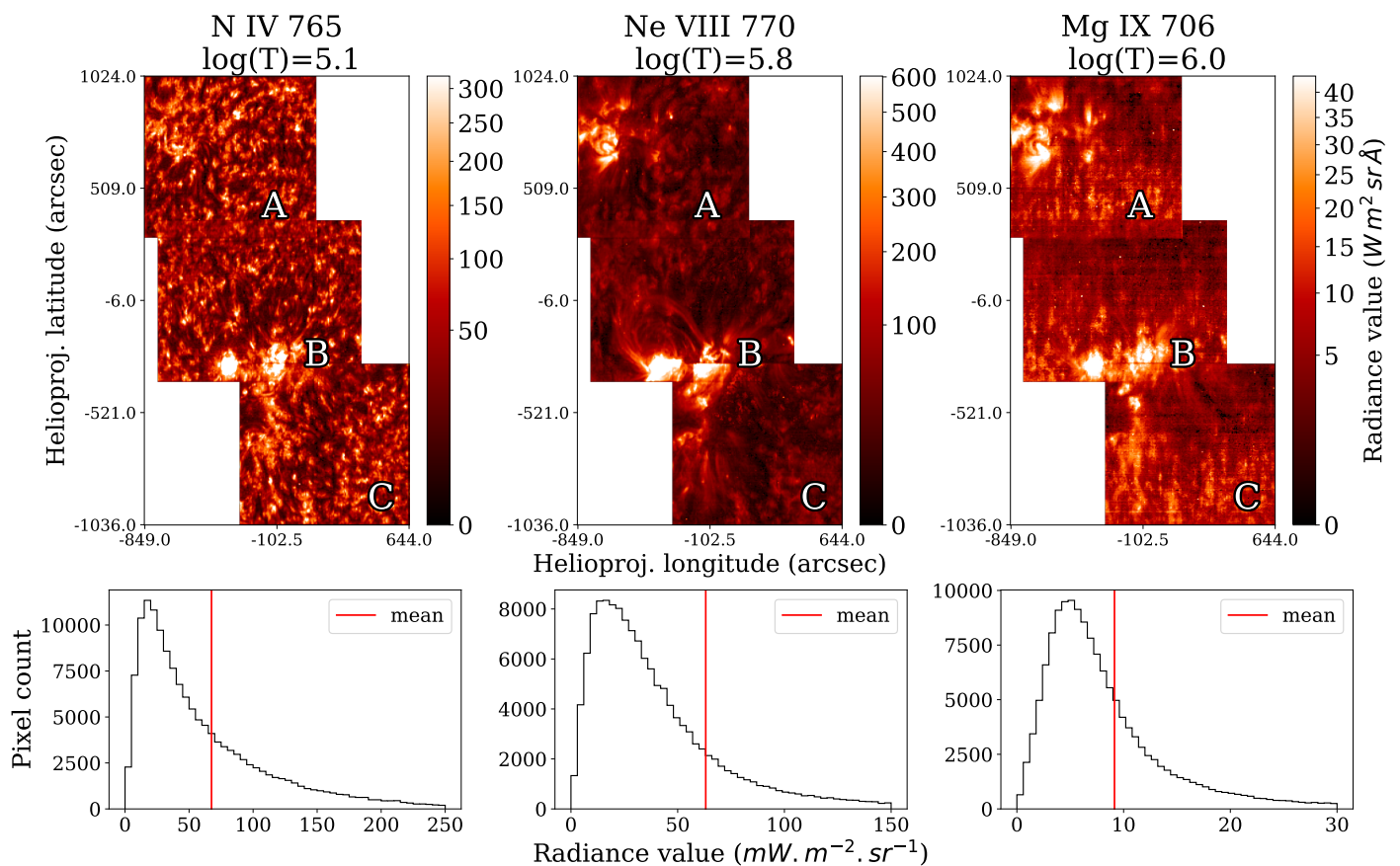


Fig. 2: Top panel: radiance maps from lines N IV 765 Å, Ne VIII 770 Å and Mg IX 706 Å. The three rasters are labeled A, B and C for more clarity. Bottom panel: histograms of corresponding radiances.

Line	SUMER QS	SPICE 2020 AR	SPICE 2022 AR S1	SPICE 2022 AR S4	SPICE 2022 QS
O III 702.8	27.5	22.3 ± 6.6	39.0 ± 7.7	139.7 ± 17.1	16.1 ± 5.3
O III 703.8	43.5	22.7 ± 6.5	35.5 ± 7.6	132.6 ± 12.9	12.2 ± 5.2
Mg IX 706	-	19.1 ± 5.1	30.2 ± 7.7	60.4 ± 14.4	5.7 ± 5.3
S IV 748	2.9	-	13.3 ± 7.3	24.4 ± 14.8	5.9 ± 1.4
S IV 750	6.9	-	17.7 ± 7.4	90.0 ± 12.1	6.2 ± 1.2
N IV 765	80.7	32.8 ± 8.6	123.7 ± 9.7	538.9 ± 16.1	55.3 ± 7.4
Ne VIII 770	73.1	67.2 ± 17.2	361.7 ± 11.5	1205.2 ± 31.1	30.3 ± 7.3
Mg VIII 772	-	10.4 ± 3.3	57.2 ± 12.0	584.5 ± 29.0	9.3 ± 1.7
S V 786	32.1	21.7 ± 6.2	77.5 ± 16.4	117.3 ± 87.5	19.1 ± 9.9
O IV 787	58.5	38.6 ± 10.3	121.1 ± 16.4	334.6 ± 86.9	31.9 ± 9.9
O I / Na VI 988.6	-	-	35.3 ± 22.9	45.4 ± 43.3	6.3 ± 14.8
N III 989.8	23.0	-	40.4 ± 22.2	175.5 ± 40.2	10.7 ± 14.5
N III 991.5	44.2	12.3 ± 4.8	120.5 ± 22.4	472.3 ± 77.4	25.5 ± 14.6
O VI 1032	354.0	273.7 ± 69.0	1562.0 ± 33.1	3419.0 ± 47.3	156 ± 17.6

Table 3: Comparison of our radiance values (see Figure 3 for the regions selected, SPICE QS including both S2 and S3) with SUMER (QS), taken from Dufresne et al. (2023) and SPICE 2020 (AR) from the region S2 of Brooks et al. (2022). Units of radiances for SUMER are in $erg \text{ sr}^{-1} \text{ cm}^{-2} \text{ s}^{-1}$ and SPICE ones have been converted to $mW \text{ sr}^{-1} \text{ m}^{-2}$, which are equivalent. Our values are corrected by a degradation factor of 2.5 and the spectral binning of the lines N IV, Ne VIII / Mg VIII and O VI has been accounted for by multiplying the radiances by the binning factor.

to match these measurements, two areas from panels A and B (S2 and S3, see Figure 3) have been selected, and the average of the intensity values have been computed. The results are presented in Table 3. Even though we tried to choose similar regions to average the radiance values, it is important to keep in mind that the Sun is an active star and that we cannot expect to obtain the exact same values, especially taking into account the current stage

in the solar cycle. The deviation of the values is significantly greater for the active regions. The sizes of the ARs observed are fairly similar, but the magnetic structures differ from AR 12781 to our AR 12958, such that AR 12781 is larger, more complex and has a stronger magnetic field. The radiance values of the cooler lines overlap within the uncertainties, but brighter, hotter

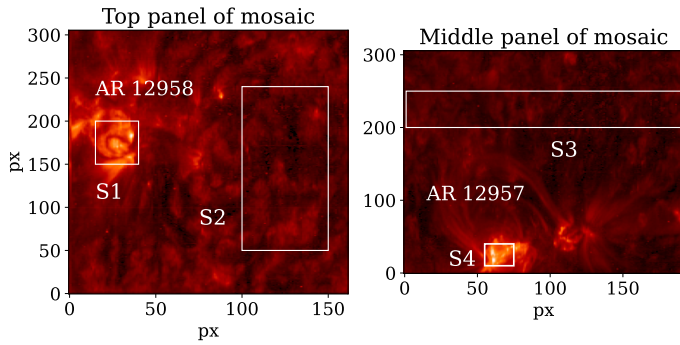


Fig. 3: Areas S1 (AR), S2 / S3 (QS) and S4 (AR), seen in the Ne VIII 770 Å line.

lines show factors of two, up to 5, which is not uncommon when observing ARs.

The quiet Sun values should show less discrepancy than the ARs, especially for lower temperature lines (Andretta & Del Zanna 2014). We are currently unable to explain the discrepancies seen in Table 3 for the QS values. One cause of these differences could be that the dark subtraction for SPICE was not very accurate for this dataset, resulting in inaccuracies in the intensities, especially for quiet Sun values, which have a lower signal. Another possibility is that the quiet Sun region selected here is not representative of the average quiet Sun. Further observations with SPICE might resolve this issue.

In summary, after applying some pre-processing to the spectra, we performed a Gaussian fitting of the emission peaks. The results of the line fitting are compared with previous SPICE and SUMER measurements, showing acceptable coherence on the relative intensity between lines for the ARs, but differences between the quiet Sun values which should be further investigated.

In the following sections, we present the diagnostic methods used to infer plasma properties from SPICE mosaic data.

3. Methods

The intensity of an optically thin spectral line, assuming a plasma in ionization equilibrium, and the abundance of an element X to be constant along the line of sight, can be defined as:

$$I(\lambda_{ji}) = \text{Ab}(X) \int_h C(n_e, T, \lambda_{ji}) n_e n_H dh$$

$$\approx \text{Ab}(X) \int_h C(n_e, T, \lambda_{ji}) n_e^2 dh, \quad (1)$$

C being the contribution function, $\text{Ab}(X)$ the elemental abundance of the element X and n_e and n_H the electron and hydrogen density, respectively. An estimation of the plasma temperature, assuming an isothermal distribution of the plasma, can be inferred from the ratio of two lines of the same element, as their ratio is directly equal to the ratio of their contribution function:

$$\frac{I_1^{obs}}{I_2^{obs}} = \frac{C_1(T_0, n_e)}{C_2(T_0, n_e)} \quad (2)$$

As defined in G. & H.E. (2018), a column differential emission measure (DEM) can be defined if a relationship exists between the temperature and the electron density:

$$\text{DEM}(T) = n_e^2 \frac{dh}{dT}. \quad (3)$$

Equation 1 can then be rewritten as:

$$I(\lambda_{ji}) = \text{Ab}(X) \int_T C(n_e, T, \lambda_{ji}) \text{DEM}(T) dT \quad (4)$$

A column emission measure can also be computed, integrating the DEM over the temperature range:

$$\text{EM} = \int_h n_e^2 dh = \int_T \text{DEM}(T) dT \quad (5)$$

The DEM represents the amount of plasma along the line of sight, making it an essential parameter for inferring diagnostics from observed radiances.

A simple estimation of the temperature distribution (first introduced by Strong (1980)) is to plot the ratio $I_{obs}/G(T)$ as a function of temperature, with $G(T) = \text{Ab}(X) C(T)$. The loci of the resulted curves represents an upper limit to the emission measure at each temperature. In an isothermal-plasma, the curves should intersect at a common point. If the plasma is not isothermal, the curves are more uniformly distributed; it is then necessary to perform a DEM analysis to obtain the distribution of plasma along the line of sight.

The EM loci method offers a simple way to measure the relative abundances of elements. It is also a far more accurate method than any other one, when the plasma is isothermal. In fact, incorrect results have been published in the literature when forcing a continuous (DEM) distribution to solar features such as active region cool loops, as reviewed in G. & H.E. (2018).

The EM loci curves for AR areas from the connection mosaic are shown in Figure 4. The computation has been performed using photospheric abundances for high-FIP elements, and different FIP bias values for the low-FIP ones – usually, a factor of 4 is adopted (Warren et al. 2016).

Caution should be taken when considering the Li-like ions (Ne VIII and O VI) as they have often been found anomalous in terms of their emission measures, as reviewed in G. & H.E. (2018). New ionization equilibria presented by Dufresne et al. (2023) improve the results, but still leave significant discrepancies between the observed and predicted intensities for some Li-like ions. The reasons are still being investigated, but could be linked to the high-temperature tail of their contribution function or time-dependent ionization.

For active region loops, the curves overlap at a unique temperature value, which is an indication of a near isothermal plasma in the area observed, as expected (see the G. & H.E. 2018, review). The values and shape of the curves are consistent with the ones found in Brooks et al. (2022), especially for the FIP bias values between 3 and 4, in agreement with Warren et al. (2016) and Baker et al. (2015). The intersection of the curves indicates a plasma temperature slightly lower than 1 MK, around $\log T = 5.8$ MK.

While quantifying the DEM should offer much more reliable information than other techniques (e.g. single line ratios), such as more accurate elemental abundances, unfortunately the DEM estimation and inversion is a complex problem; it is very difficult to estimate the DEM properly, especially when using an automated method. Issues have already been investigated and discussed by Judge et al. (1997), Del Zanna et al. (2002), Guennou et al. (2012a), Guennou et al. (2012b) and G. & H.E. (2018). We were also unable to de-blend some of the SPICE spectral lines used to infer the DEM, and thus we might be overestimating their radiances. Several additional lines were included for the computation of the contribution functions in order to take into account

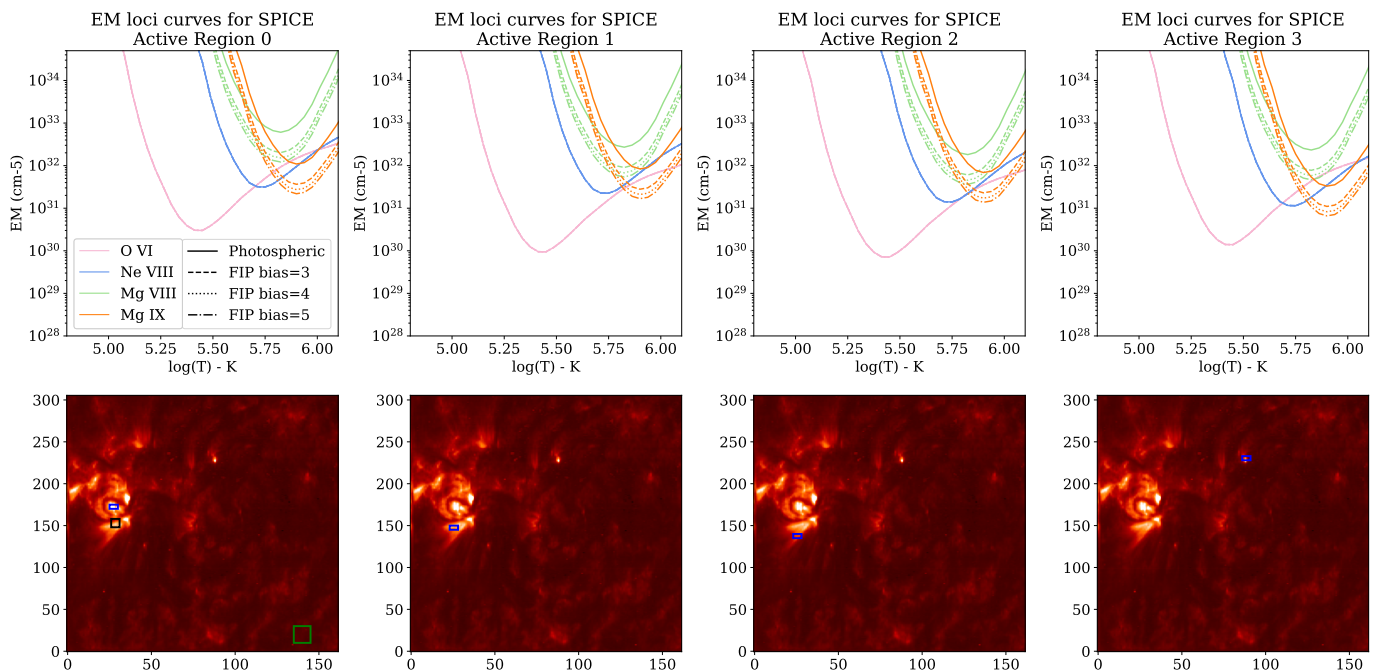


Fig. 4: EM loci curves for high temperature lines of SPICE. Blue rectangles on the maps denote the area over which the curves are computed. For the active regions, curves of low-FIP elements are plotted with different FIP bias values (1,2,4 and 5). The intersection of the curves (especially for a FIP bias of 4) indicate an isothermal plasma around $\log T=5.8$. The black and green boxes on the bottom left panel are respectively the areas chosen to compute the DEM for AR and QS region depicted in Figure 5.

the blends present in our set of lines. In addition to that, uncertainties, both random and systematic, and limited temperature resolution make the inference of the DEM even more challenging (Judge et al. 1997; Brown et al. 1991).

This problem therefore needs strong constraints, which are set in our case by using the strongest available lines of low and high FIP: O III, Mg IX, N IV, Ne VIII, Mg VIII, S V, O IV and N III. This set of lines gives us good constraints at lower temperatures, but lacks some high-temperatures ones. In further work, using the HRI 174 Å band from EUI could provide a good, reliable high-temperature constraint for the DEM.

For this work, we used a recent method for DEM reconstruction (Plowman & Caspi 2020), which showed satisfying results on SDO/AIA data. The temperature range used for the DEM inversion is $10^{4.7}$ to $10^{6.2}$ K with a temperature bin size of $\Delta(\log T) = 0.035$ K.

As a simple test of the accuracy of our results, we can compare the usual DEM shape within an active region to the one we compute over AR 12958. The DEMs which we computed are intended to give an indication of which lines contribute the most to SPICE's spectra under different solar conditions (CH, QS, AR).

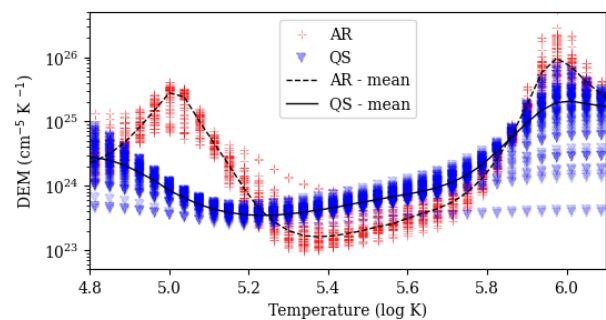


Fig. 5: Distribution of the DEM with temperature over a QS and AR area. The QS curve has a flatter, more multithermal-like shape, whereas the AR curve has two clear emission peaks. For regions selected, see Figure 4.

The distribution of DEM values according to temperature in this active region is shown in Figure 5.

The peak (bell-shaped) coming from the AR emitting at $\log T = 6.0$ is what we would expect for our temperature range and the lines chosen – a higher temperature is observed over the active region targeted. The DEMs over a QS area present a large local minimum above $\log T = 5.2$ and a peak above $\log T = 6.0$ as seen in (Raymond & Doyle 1981). We also observe an increase as it reaches chromospheric temperatures, as described in G. & H.E. (2018). Caution should be taken when treating the low-temperature tail of the DEM distribution, as it is directly constrained by low-temperature lines that may be influenced by opacity effects. Another issue is that the two strongest lines used in the DEM inversion are Li-like ions, which have a significant contribution at temperatures higher than the peak ones, due to the ionization fraction tail resulting from dielectronic recomb-

nation. Anomalies are discussed in Del Zanna et al. (2002) and references therein.

In the next section, we conduct further analysis based on the concepts presented previously, involving solar active regions description, temperature diagnostics, and comparison with EU1 data and future *in-situ* HIS data.

4. Preliminary diagnostics and comparison with other instruments

4.1. Comparison with EU1 data

On the very same day, the Extreme UV Imager (EUI) instrument recorded synoptic and high-resolution images. EUI has three telescopes: the Full Sun Imager (FSI), which records images at two wavelengths (174 and 304 Å), and two high-resolution imagers. The FSI images were taken with a frequency of one image every 900 seconds.

In order to check the accuracy of our line fitting results, we compare the SPICE data with the EUI on Solar Orbiter images. The higher resolution of EUI images allows for linking of precise structures to the composition measurements of SPICE. However, EUI images are recorded almost instantly while SPICE's rasters are recorded over several hours, which causes an alignment problem between the two resulting images. To address this problem, we used the `reproject` package available in Python (Robitaille et al. 2023), and added to it an empirical ad-hoc offset to clear out any remaining misalignment. The results of this reprojection are presented in Figure 6. We selected approximately co-temporal FSI images, and the SPICE spectral lines plotted on top of EUI images have been chosen so that the temperature of the ions observed match. For the EUI 304 Å which corresponds to He II ($\log T = 4.9$), SPICE's O III 702.8 Å ($\log T = 4.9$) is superimposed. The targeted region on this left panel is the photosphere and the lower transition region. As for EUI 174 Å (Fe X, $\log T = 6.1$), SPICE's Mg IX 706 ($\log T = 6.0$) is superimposed, despite its low SNR. In the latter, we look for upper transition region and coronal activity. The superpositions show very good consistency: we observe the same texture patterns on the QS areas and the active regions' shape and location match almost perfectly. We look forward to comparing future SPICE images with HRI images in order to get more detailed comparisons. These superpositions nonetheless require further processing (we applied a Contrast Limited Adaptive Histogram Equalization (CLAHE) on the normalized image, which performs local contrast enhancement using histograms computed over different tile regions of the image) in order to match the contrast of the two images; especially for the higher temperatures Fe X/Ne VIII which have narrower bands.

4.2. Back-mapping with *in-situ* data

The comparison of SPICE abundance ratio maps with *in-situ* HIS abundances offers a potential avenue for confirming the magnetic connectivity between the solar wind observed at a given instrument location and the wind sources on the Sun. *In-situ* measurements are all the more important because once the solar wind plasma leaves the Sun (above 1.5 solar radii), abundances are not affected by any fractionation (or FIP effect) processes, opening an independent window for composition diagnostics (Baker et al. 2019; Parenti et al. 2021). However, remote and direct measurements need to be connected since they do not record the same events at the same time. Previous studies in-

volving data from the SWICS instrument on board of *Ulysses* and ACE satellites could be used as reference points.

In order to correctly back-map the events observed with remote sensing instruments, we need to take into account the delay between the two observations of the same event. To model the connectivity of Solar Orbiter, we used the MADAWG connectivity tool (Rouillard et al. 2020). The coronal magnetic field is reconstructed by the tool using the potential field source surface (PFSS) model, and then extended assuming a Parker spiral model. The tool provided an estimated propagation time of two days and 6 hours between the Sun and Solar Orbiter. The evolution of AR 12957 and AR 12958 can be followed with the tool, as shown in Figure 7, including the solar wind footpoint speed. The SW speed forecast increases starting at 545.2 km/s on March 1st, reaching 610.3 km/s at the time of SPICE's observations, and then decreasing to 475.7 km/s on March 3rd. SolO's connectivity point stays connected to the boundary of AR 12957, first to the negative polarity and moving on to the second negative polarity of the active region, adjacent to an equatorial coronal hole. The radial magnetic field measured by MAG supports this as it is predominantly negative throughout the time period.

The HIS and SPICE instruments have a wide range of joint observations, as HIS measurements can include He¹⁻²⁺, C²⁻⁶⁺, N²⁻⁷⁺, O²⁻⁸⁺, Ne⁶⁻⁹⁺, Mg⁶⁻¹²⁺, Si⁶⁻¹²⁺, S⁶⁻¹⁴⁺, and Fe³⁻²⁴⁺. Consequently, when SPICE and SWA/HIS are employed together, the intensities recorded by SPICE can be used to validate the solar wind model predictions in the transition region and low corona. Meanwhile, HIS measurements can assess the predicted charge states *in situ*, as explained in Fludra & Landi (2018). Unfortunately, SWA/HIS data corresponding to the dates of SPICE connection mosaic observations are largely incomplete. An example of an analysis panel of SWA/HIS data is shown in Figure 8. The data displayed show the evolution from March 1st 2022 to March 6th 2022. At the moment, we are unable to draw any conclusions in regards to connectivity given these gaps in the data. However, SPICE and HIS can offer the capability to determine the abundance ratios of low-FIP and high-FIP elements (e.g., Fe/O, S/N, Mg/Ne). By comparing the abundance ratio maps obtained by SPICE with the *in situ* abundances measured by SWA/HIS, it would be possible to verify the magnetic connectivity between the solar wind observed at the spacecraft's location and the solar sources of the wind.

We also expect HIS data to provide elemental composition and ionic and proton temperature signatures for the active regions we observed. In particular, higher values of the ratio O⁷⁺/O⁶⁺ (indicating higher coronal temperatures), and higher ionized elements are expected, as well as distinct peaks in speed and density corresponding to the flares observed. To compare charge states between HIS and SPICE, it is necessary to consider their measurement altitudes and the freeze-in phenomenon (Rouillard et al. 2020). The HIS measurements capture charge states at altitudes above the freeze-in region, while SPICE measurements occur below this region. To bridge the gap, additional information from a coronal electron temperature model is needed. We also look forward to comparing our abundance ratios (especially Mg/Ne, O/Ne, the latter being dependent of the solar wind speed) with their HIS equivalents. However, we do not expect a massive change in high-FIP elements relative abundances, and only a subtle one for low-FIP elements. Going forward, we expect to have more complete HIS data sets to compare with future SPICE mosaic observations.

SPICE images (O III 702.8 Å and Mg IX 706 Å)
superimposed on EUV FSI 304 / 174 Å images

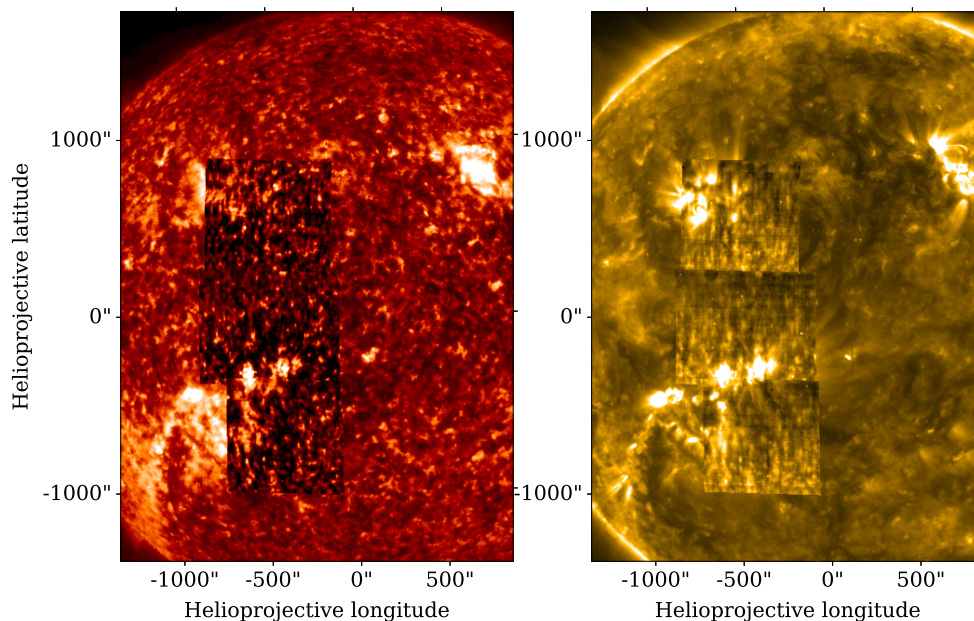


Fig. 6: Left panel: SPICE O III 703 Å superimposed on EUV FSI 304 Å. Right panel: SPICE Mg IX 706 Å on top of EUV 174 Å FSI image.

4.3. Temperature diagnostics

Temperature diagnostics can be obtained by using a ratio of two lines coming from the same element at two different ionization stages, if their contribution function does not depend on density, and assuming an isothermal plasma ($T = T_0$) along the line of sight. This assumption has to be taken with caution, as it is valid only for specific regions (e. g., active region loops). The isothermal assumption being made, a temperature T_0 can directly be deduced from the ratio (see Eq. 2).

We required the signal-to-noise ratio to be sufficient (even though the high-temperature lines are quite noisy) and the logarithm of the temperature to be between $\log_{10}(T) = 4.7$ and 6. The lower limit is to avoid any optical thickness effects, and the upper limit is the highest temperature observable by SPICE during these observations.

A small selection of lines observed by SPICE can be used for temperature diagnostics via line ratios; Mg IX is an excellent candidate to measure the averaged corona around 1 MK (G. & H.E. 2018), in combination with the B-like Mg VIII, although the line from Mg VIII as a slight (20%) density sensitivity. The ratio from C-like O III to B-like O IV could also maybe be investigated, being also dependent on temperature and very little on density. However, the temperature distribution seen in DEM is very broad: the temperatures extend from 30,000 K to 1 M K. Thus, the temperature value from the O IV/O III ratio would only represent one temperature value sampled from a very broad range, and not the temperature of the transition region plasma.

The line ratio method restricts the range of temperature solutions to $T_1 \leq T_0 \leq T_2$ (T_1, T_2 being the limits where the contribution functions of lines 1 and 2 are less than 1% of their values). The range of constraint is presented in Figure 10 for the magnesium.

The reliability of the magnesium ratio is limited to active regions, due to very low signal to noise ratio in quieter areas.

On the right panel of Figure 9, the temperature diagnostic inferred from the two magnesium lines shows typical behavior, as a cooler temperature T_0 at the footpoints of the ARs and higher temperatures where upper transition region / coronal material is expected. Hotter regions are where we observe more coronal-like loops and brighter regions, as seen with EUV 174 Å.

Three points are important to note: (1) those temperature maps are no more than a weighted average of the contribution functions and the emission measure; (2) the contribution functions inferred from the CHIANTI database overestimates the formation temperature of the ions involved here (Dufresne et al. 2023); (3) The accuracy of the temperature diagnostics relies on the reliability of the ionization/recombination rates and, most importantly, on the ionization equilibrium assumption. Those assumptions are acceptable in the corona but questionable in the transition region due to shorter dynamical timescales regarding recombination rates (G. & H.E. 2018), especially around strong magnetic features. However, we find the temperature maps to be consistent with what we expect to see at these temperature ranges and they therefore provide useful information.

Throughout the last sections, we have given an overview of which analyses and diagnostics are likely to be most appropriate with SPICE data. These includes radiance maps for distinct lines, intensity ratios for elemental composition, temperature diagnostics, and cross-analysis with other SolO instruments (EUV and HIS). While comparing elemental abundance data with other instruments is one of SPICE's main features, we can get a direct analysis of the abundance patterns by studying the FIP effect through SPICE-only data which we will do in the following section.

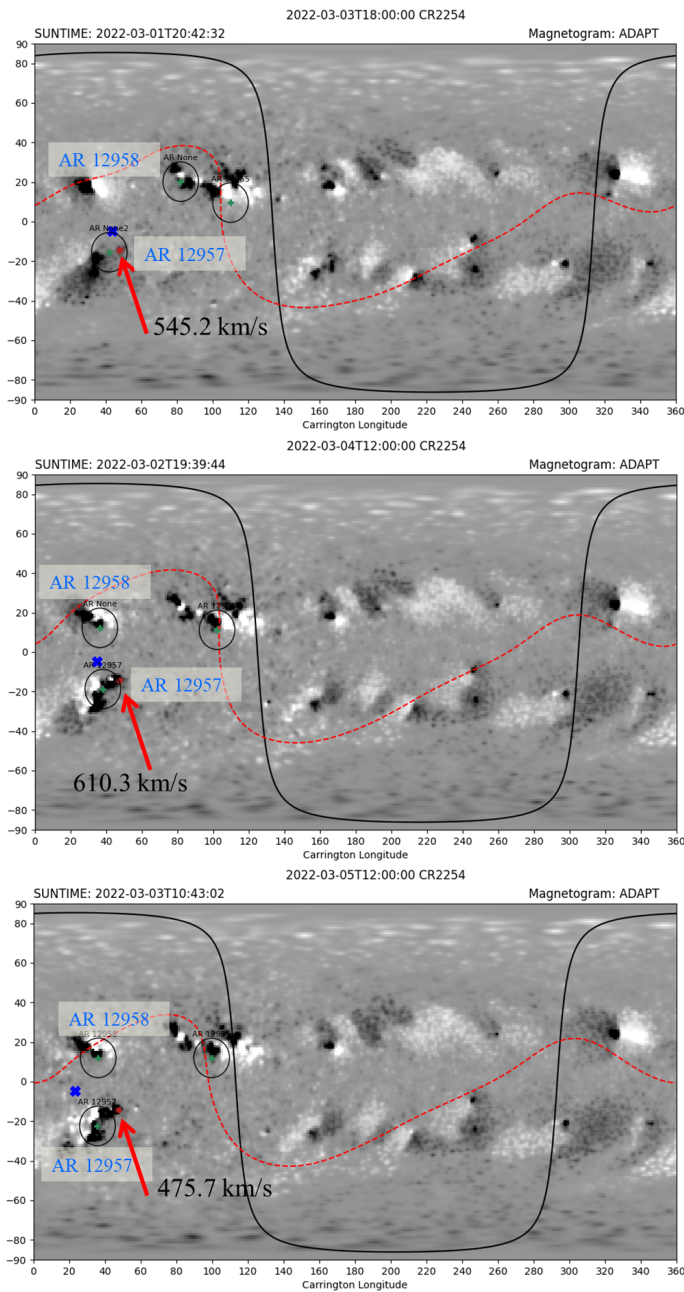


Fig. 7: Connectivity maps from the MADAWG Connectivity Tool, from March 1 2022 to March 3 2022. The maps are plotted over ADAPT magnetograms. The blue cross represents the sub-spacecraft point, and the red dot (pointed by the red arrow) the footpoint of the measured solar wind. The red dashed line represents the Heliospheric current sheet, and the black solid curve the visible disk from SOLO.

5. Relative abundance diagnostics from line ratios and DEM methods

We define the FIP bias f_X in the corona as

$$f_X = \frac{Ab_X^C}{Ab_X^{Ph}}, \quad (6)$$

where Ab_X^C and Ab_X^{Ph} are the coronal and photospheric abundances of element X , respectively. SPICE observes lines from one low-FIP element (Mg), the intermediate-FIP element S, and

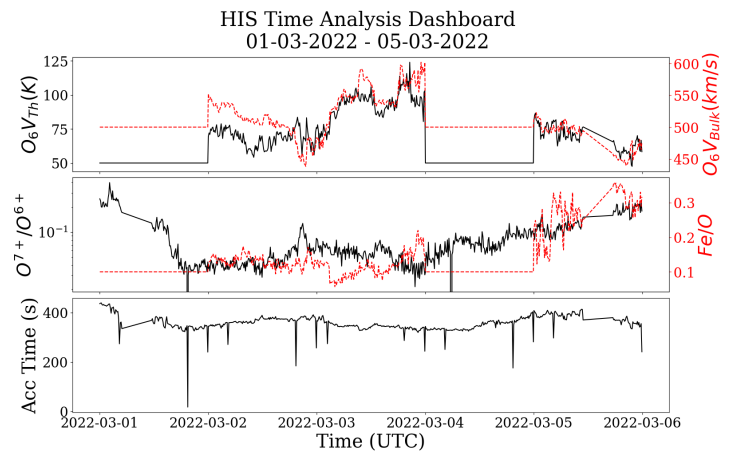


Fig. 8: Multi-panel plot from HIS data recorded from March 1st 00:00 UTC to March 5th 00:00 UTC. Top panel: O^{6+} thermal and bulk velocity, middle panel: O^{7+}/O^{6+} ratio and elemental Fe/O ratio, bottom panel: summed accumulation time for this time step, equal to the total measurement time for each elevation step throughout the accumulated scans (less measurement time from elevation steps that have not passed quality filtering).

the high-FIP elements N, O and Ne. Values of FIP bias around 1 are expected for coronal holes and sources of fast solar wind, while higher values (2-5) would indicate sources of slow solar wind and active regions.

In selecting the lines which would be used for FIP bias computation, we have chosen those that best correspond to the four constraints defined by Feldman et al. (2009) for Hinode/EIS lines, which are the following:

- Consider only the lines with an upper atmosphere or coronal temperature ($\log(T) \gtrsim 5$),
- have a minimum brightness according to the CHIANTI database ($\text{Int} \geq 10^3 \text{ erg cm}^{-2} \text{ sr}^{-1} \text{ s}^{-1}$), and no blended lines if possible,
- narrow down to lines with transitions between the first excited and ground configurations,
- and lastly, focus solely on lines with a low electron-density dependency.

The chosen lines and their transitions are reported in bold in Table 1.

Typically, one tries to determine the relative FIP bias in the solar atmosphere of two elements from the ratio of the radiances of two spectral lines (one for each element). The ratio of the FIP biases of these elements can be written in the coronal approximation (Zambrana Prado & Buchlin 2019) as:

$$\frac{f_{X_{LF}}}{f_{X_{HF}}} = \frac{I_{LF}}{I_{HF}} \left(\frac{Ab_{X_{LF}}^{Ph} \langle C_{LF}, \text{DEM} \rangle}{Ab_{X_{HF}}^{Ph} \langle C_{HF}, \text{DEM} \rangle} \right)^{-1}, \quad (7)$$

where I_{LF} and I_{HF} are the radiances of the lines used for the diagnostics, low and high-FIP respectively; C_{LF} and C_{HF} are the corresponding contribution functions and $\langle a, b \rangle \equiv \int a(T) b(T) dT$.

All the atomic physics contributing to the emission of the ions is contained in the contribution functions. The DEM is tied to the distribution of plasma with temperature along the line-of-sight.

One then can do, for example, one of three following methods:

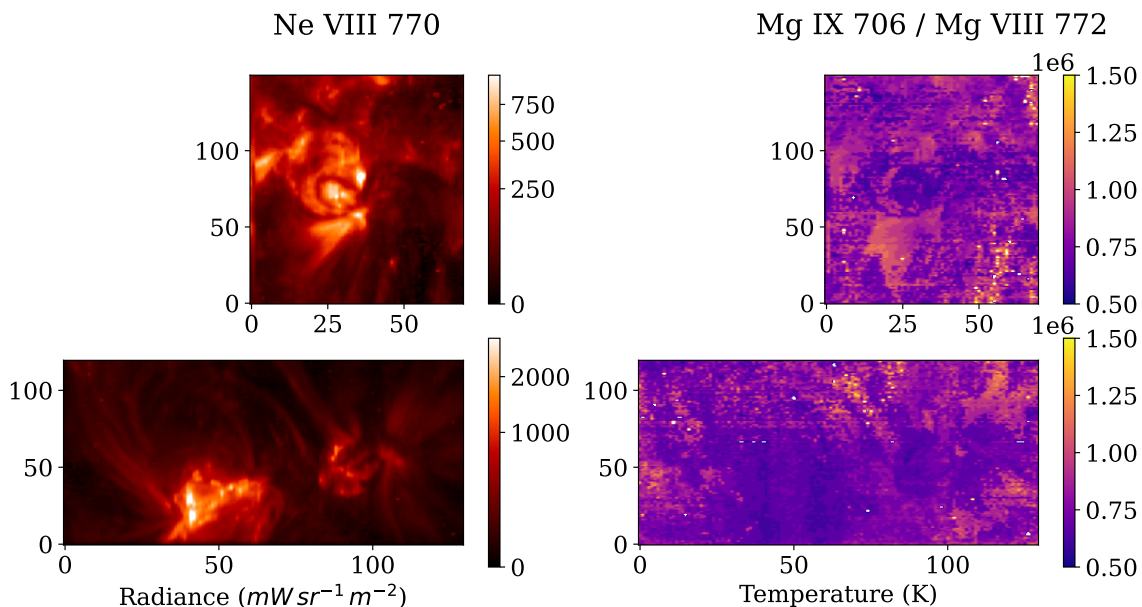


Fig. 9: Left panel: radiance map from the line Ne VIII (units in $\text{mW sr}^{-1} \text{m}^{-2}$). Right panel: temperature diagnostic maps from element Mg. Top row shows AR 12958, bottom row shows AR 12957.

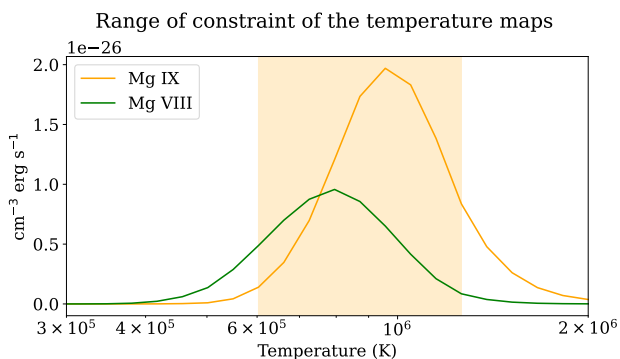


Fig. 10: Range of constraints of the temperature maps based on the contribution functions. Left: oxygen diagnostic; right: magnesium diagnostic.

- Find two lines with contribution functions similar enough that the ratio $\langle C_{\text{LF}}, \text{DEM} \rangle / \langle C_{\text{HF}}, \text{DEM} \rangle$ is constant, which we will call the 2LR (two-line ratio) method.
- Determine the DEM in order to compute the ratio of Equation 7, also called the DEM inversion method.
- Use a linear combination of spectral lines optimized for relative FIP bias determination. This is the linear combination ratio (LCR) method developed in Zambrana Prado & Buchlin (2019).

We will use these three techniques to determine the relative FIP bias in our observations.

5.1. Two-line ratio method

The 2LR method has been widely used for computing FIP bias maps (Mohan et al. 2000), but its problem resides in its reliance on very strong assumptions and hypotheses. In fact, any two lines involved must have very close formation temperatures and contribution functions – to the extent that they can be approximated by the ratio of their maxima (Zambrana Prado & Buchlin

2019). In real-world data, no two contribution functions are exactly the same; there is always at least a small dependence on the DEM. Besides that, unfortunately, the interesting lines recorded by SPICE for FIP diagnostic have very few similarities regarding their contribution functions.

Magnesium-neon is a couple which best meets the requirements stated above (Widing & Feldman (2001)). Neon acts as a (very) high-FIP (HF) (21.6 eV) representative, while magnesium (7.6 eV) is a representative for the low-FIP (LF) group. Widing & Feldman (1989) suggested the use of a simplification where the emission measure factor is canceled out by the ratio, and the relative FIP bias can simply be written as:

$$\frac{f_{\text{LF}}}{f_{\text{HF}}} = \frac{\max(C_{\text{HF}}) Ab_{\text{HF}}^{\text{Ph}} I_{\text{LF}}}{\max(C_{\text{LF}}) Ab_{\text{LF}}^{\text{Ph}} I_{\text{HF}}}, \quad (8)$$

where $Ab_{\text{X}_{\text{LF}/\text{HF}}}^{\text{Ph}}$ is the (established) low-FIP / high-FIP photospheric abundance of element X_i , $\max(C_{X_i})$ is the maximum of the contribution function of the ion X_i and I_{X_i} is the observed intensity of element X_i .

The line pairs involving the neon, magnesium, sulfur and nitrogen lines are thus the ones which received the most attention in this work. We extracted two magnesium lines (Mg VIII 772 Å and Mg IX 706 Å) and the single neon line available (Ne VIII 770 Å). These pairings are particularly interesting in the sense that the three ions (the two Mg ions and Ne) are formed at relatively high temperatures (respectively 0.8 MK, 1 MK and 0.63 MK), and are respectively low and high FIP elements (7.6 eV and 21.6 eV), which makes them very good candidates for meeting the assumptions of section 5 (Brooks et al. 2022). The FIP gap and close peak temperatures are the two main characteristics we look for when choosing a line pairing, but close contribution functions and good signal to noise ratio should also be taken into account. However, magnesium and neon do not have a good overlap temperature-wise (see Figures B.1 and B.2) and if not properly modeled, the measured FIP bias can be affected by the significant high-temperature tail of Ne VIII. The signal of the magnesium lines is also very weak outside the active regions;

that is why the FIP bias measurements with these lines should only be trusted in those regions.

While interesting, neon is a challenging element, since it has a noble gas configuration—hence its very high FIP—and is thus present in the photosphere mainly in its neutral form. As a result, no spectral lines for measuring the neon absolute abundance are available.

Satisfying results have also been obtained with the pairing sulfur (low-FIP) / nitrogen (high-FIP), even though sulfur is an intermediate FIP element. SPICE also observes a wide variety of lines of those two elements, which leads to more consistent analysis.

Presented in Figure 11 are the results we obtained by applying the two-line ratio method (i.e., Equation 8) which gave the best results. The contribution functions were computed with an assumed electron density of $n_e = 2 \times 10^9 \text{ cm}^{-3}$.

The magnesium is highly enhanced in the regions where there is magnetic activity, especially at the footpoint of the AR 12957, which is consistent with the fact that previous observations from Hinode showed that edges of active regions are very good candidates for sources of slow solar wind, hence should show high relative FIP values. The darker purple areas show low-FIP enhancement, so are a potential source of slow solar wind. Similar trends are observed with the ratio S/N, the latter having the advantage of being less sensitive to temperature – in contrary to the ratio Mg/Ne, thermal structures are less distinct, due to closer formation temperatures. AR 12958 shows less clear enhancements, however higher values are observed in the area circled in black, particularly at the bottom right on the right panel.

The values of these line ratio maps are however to be taken with caution, as the 2LR method relies on many assumptions. The Widing and Feldman method can in fact produce incorrect results, if the plasma is not emitted at the peak of the $C(T)$, which is often the case (see discussion and references in G. & H.E. 2018). Moreover, as suggested by Warren et al. (2016), if physical mechanisms causing the FIP effect are averaged over time, which is the case with the relatively long SPICE exposures, the active regions might show a smaller value of FIP bias compared to older and long-lasting coronal structures.

5.2. DEM inversion

We computed the relative FIP biases following Equation 9, $\langle a, b \rangle$ being the scalar product defined as $\sum_{i=1}^n a_i b_i$, $a, b \in \mathbb{R}^n$.

$$\text{FIP}_{\text{Bias}} = \frac{I_{LF}}{I_{HF}} \left(\frac{A_{LF}^{Ph} \langle C_{LF}, \text{DEM} \rangle}{A_{HF}^{Ph} \langle C_{HF}, \text{DEM} \rangle} \right)^{-1} \quad (9)$$

Several combinations of lines were tried, but most of them showed inconsistent results. The best result of the FIP bias values computed with the DEM is presented in Figure 12, with the same layout as in Figure 11. Thermal effects are still strong, despite the use of the DEM (the loop of AR 12957 is clearly distinguishable when using the neon and magnesium ratios, very likely due to the difference in their contribution functions (their peaks are more than 300 000 K apart for Mg IX / Ne VIII, 100 000 K apart for Mg VIII / Ne VIII). In spite of these thermal structures, we still observe a uniformity in the relative FIPs, namely higher values at the footpoints of the loops and certain uniformity in quiet areas. To compensate the very low signal-to-noise ratio of the line Mg VIII, we show on the middle panel the ratio of the sum of the two magnesium lines to the neon one. FIP bias shouldn’t be affected too much by the degree of ionization, since the value is elemental. This method doesn’t seem to show

X	FIP (eV)	A_X^C	A_X^P	f_X	f_S/f_N
S	10.36	1.69×10^{-5}	1.32×10^{-5}	1.28	1.42
N	14.03	5.17×10^{-5}	6.76×10^{-5}	0.78	

Table 4: First ionization potential of sulfur and nitrogen, their coronal and photospheric abundances taken from Schmelz et al. (2012) and Asplund et al. (2021) respectively, their abundance biases, and the corresponding relative abundance bias.

very good consistency of AR 12958, however, it seems to identify precise areas of low-FIP enhancements. No solid conclusion can be drawn at this point, but it might be an encouraging way to compensate the low signal of SPICE’s low-FIP elements.

A further improvement could be using temperature maps from other instruments such as Hinode/EIS to better constrain higher temperatures.

5.3. Linear Combination Ratio

We summarize here the principle of the Linear Combination Ratio method that is explained in detail in Zambrana Prado & Buchlin (2019).

Improving on the 2LR method, the LCR method uses two linear combinations of lines rather than only two lines. The resulting linear combinations of the contribution functions for low-FIP and high-FIP elements provide a better estimate of the relative FIP bias and render the method DEM-independent. Using individual lines i of low-FIP elements on one hand and j of high-FIP elements on the other hand, we build linear combinations of their radiances I_i from:

$$I_{LF} \equiv \sum_{i \in (LF)} \alpha_i \frac{I_i}{A_i^P} \quad \text{and} \quad I_{HF} \equiv \sum_{j \in (HF)} \beta_j \frac{I_j}{A_j^P}, \quad (10)$$

where α_i or β_j is a coefficient for line i or j . These coefficients are optimized in order for the method to be as DEM-independent as possible (see details in Zambrana Prado & Buchlin (2019) and Zambrana Prado et al. (in prep.)). A Python module has been developed and is freely available at <https://git.ias.u-psud.fr/nzambran/fiplcr>. It can be used to compute the optimal coefficients α_i and β_j to obtain accurate relative FIP bias maps from observations, without the need for computing the DEM.

Sulfur is considered to be a low FIP element for this diagnostic since no low FIP elements show spectral lines in the same temperature range as the selected N III and N IV lines. Table 4 lists the photospheric abundances we used to compute the relative FIP biases, taken from Asplund et al. (2021). It lists as well the coronal abundances from Schmelz et al. (2012) and the corresponding relative abundance bias which are only informative, to allow us to see in which areas we will obtain coronal abundances in our relative FIP bias maps. Table 5 shows the optimized coefficients obtained for each line and used in our calculations.

For all mosaic rasters, relative FIP bias maps were computed using the LCR method. They are depicted in Figure 13. The top of the figure shows the obtained relative FIP bias map and the bottom shows the histogram of the obtained values. The colormap of the histogram corresponds to the values in the maps, and white pixels correspond to pixels where the fitting of any of the four lines was not satisfying. The obtained histograms peak near the photospheric value of reference, which is reassuring since a lot of the observed plasma is QS plasma and therefore is expected to have a mostly photospheric FIP bias. We see small

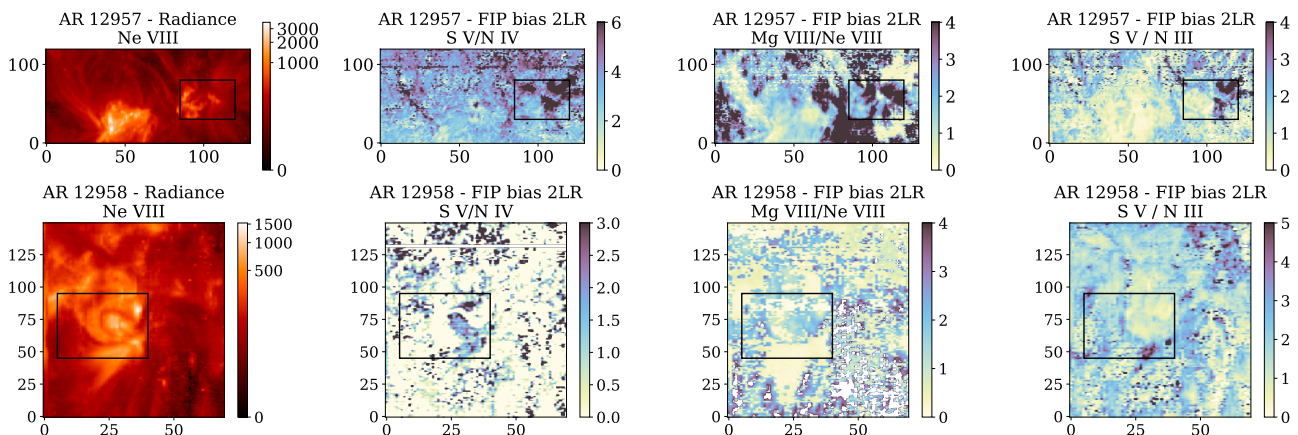


Fig. 11: FIP bias diagnostic using the 2LR method. The top panel represents the active region observed in panel B of the mosaic, and the bottom panel is a zoom over the active region observed on panel A of the mosaic. White pixels are areas where the signal was too low to draw any conclusions on the diagnostic result. The boxes are used as a reference to relate the FIP maps to the radiance maps. Darker areas suggest higher FIP-bias values, therefore coronal-like abundances and potential sources of slow solar wind.

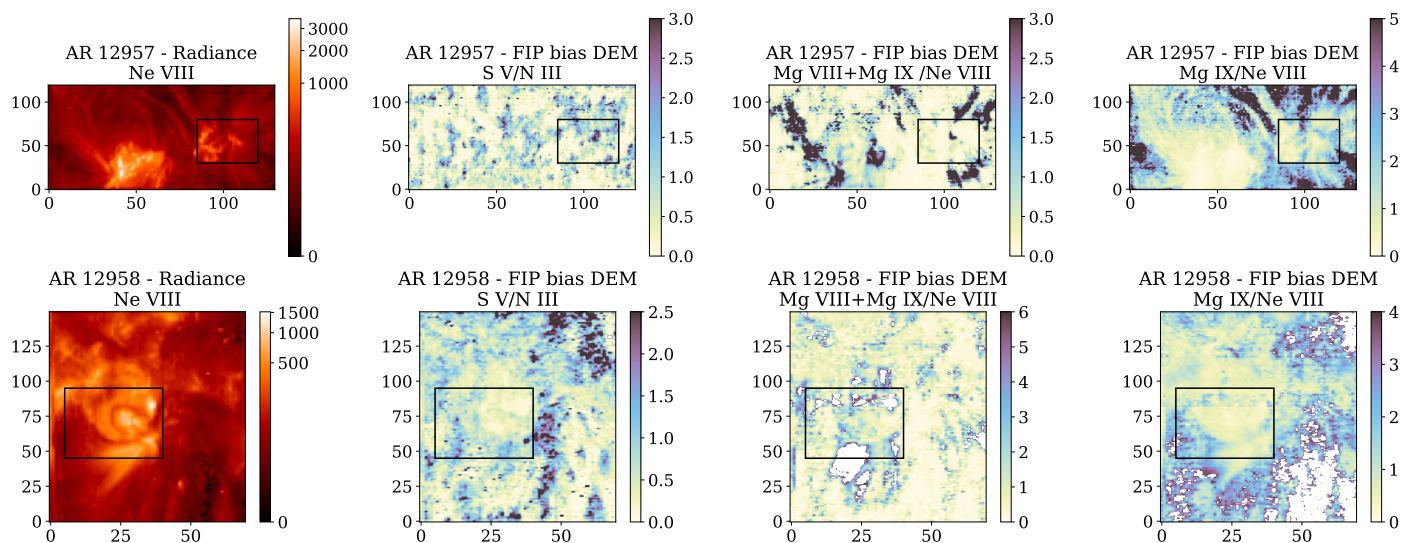


Fig. 12: Relative FIP bias maps computed with the DEM method. Regions are the same as in Figure 11. White pixels denote the same as in Figure 11.

Spectral line Wavelength in Angstroms	Coefficient
N III 991.577	1.0
N IV 765.152	2.0
S IV 750.221	3.2
S V 786.468	0.47

Table 5: α and β coefficients defined in Eq. 10 for each used spectral line, computed for $\text{Log}(n_e) = 9.5$.

areas of higher relative FIP bias, mainly around the footpoints of the loops of the ARs as well as in the center of the ARs, which is consistent with the fact that the abundance of low FIP elements is enhanced in areas where the magnetic field is closed. There is also an enhancement of the relative FIP bias in the fan loops in the AR that is in the center mosaic image.

In spite of the binning of the spectral cube and the patchiness of the fitted radiance maps, which leads to some white areas in the relative FIP bias maps, we find that the LCR FIP bias map

obtained provides useful information on the FIP biases in the coronal structures in the field of view, which is remarkable given that it was produced without any DEM inversion and only four spectral lines.

6. Discussion

SOOPs mosaics are designed to obtain a detailed map of the spatial distribution of solar atmospheric composition across an extended area of the Sun. One of their main goals is to link the remote sensing observations from Solar Orbiter with its in-situ data, especially with the SWA/HIS instrument, in order to link the in-situ events observed with their source regions on the Sun. Using this SPICE mosaic, which is the first of its kind, we have been able to explore a range of analyses and diagnostic techniques that can be performed using such spectroscopic raster data, as well as performing some preliminary processing to set standards for future observations.

Despite working with the best available calibrated data, we encountered several problems while working with SPICE data,

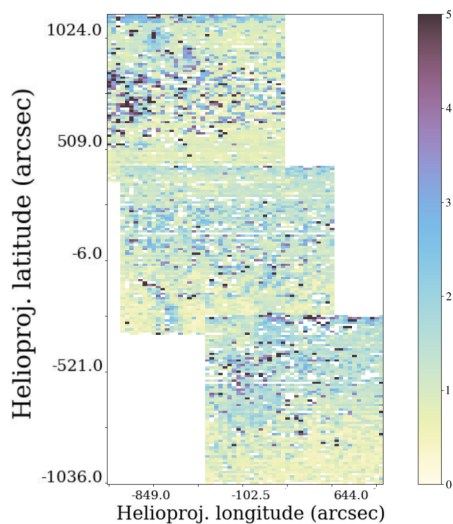


Fig. 13: Relative FIP bias computed with the LCR method. The images have been binned by a factor of 3 along the X axis and by a factor of 6 along the Y axis. The values of the relative FIPs are as expected; around 1 in Quiet Sun areas, with higher values in active regions, especially around emerging areas.

particularly concerning dark subtraction. The pipeline incorporates an automated algorithm designed to select the most appropriate dataset for dark current subtraction. By identifying the dataset closest in time to the observations, this algorithm generally yields highly accurate outcomes. However, it has come to our attention that the algorithm encountered difficulties in accurately matching the data during the period of 2-6 March 2022. This discrepancy can be attributed to temperature fluctuations in the instrument's detector that occurred on 1-2 March. Notably, these composition maps generated on March 2, 2022 employed lengthy exposures of 120s, exacerbating the issue compared to shorter exposures.

The impact of a mismatched dark subtraction is intricate in nature. While it is expected to have a negligible effect on strong or bright lines, its influence on weak or faint lines will be proportionally greater. As a result, the observed line ratios can be significantly altered as a consequence of this disparity. The degradation of the data makes this survey an important milestone as the data recorded in March 2022 will not be reproduced, or with an increasing degradation factor.

Despite those issues, radiance maps show satisfying agreement with their higher resolution counterparts taken from EU1, not only in active and hot regions, but also in quieter areas and coronal holes, where the visual texture of these regions matches between the two instruments. This result is very encouraging for future observations, and reinforces SPICE's ability to track detailed solar structures; this despite the spatial binning we currently employ. We believe we have clearly demonstrated the capability of SPICE observations to complement in-situ and other observations. Regarding the lines available, some blends are still unresolved (e.g., S IV 750 Å and Mg IX 749.5 Å), and we are limited by the small number of high-temperature lines (peaking around 1 MK). Having more of those higher-temperature lines could enable us performing more accurate temperature and density diagnostics by adding more constraints to the problem, typically in DEM inversion. Another issue concerning the DEM calculation is that fixed photospheric abundances are assumed in the computation process. But if coronal plasma is observed

along the line of sight, the lines are brighter than they would be with photospheric observations, therefore the model will tend to underestimate the line emission in those lines. It will try to compensate this incoherence by increasing the EM. This effect is, however, limited by constraints applied by other lines which are not affected by this issue, and it happens that it is the case for most lines used for DEM computation. The overall effect we observe is that the DEM is higher in certain temperature ranges, to compensate for the weakest lines in the model.

A way to address this issue would be to iterate the DEM computation, starting with photospheric abundances and adjusting them at each iteration until convergence. We could use EU1 174 Å data to add a high-temperature constraint (the 174 Å channel is dominated by Fe X, $\log(T)=6.1$), and possibly STIX data.

Even though retrieving HIS data is still a work in progress because of calibration issues of the instrument and in-flight anomalies and complicated quality evaluation due to SSD noise signatures, we plan in future works to compare in-situ and remote-sensing data and to recover the relative elemental abundances of common observed elements as well as their speed. The purpose of merging these two types of data is to perform back-mapping of heliospheric mechanisms. We seek changes in the chemical compositions, but also in velocity and ionization level measurements. Sulfur might be the key to searching for open fields (Reames 2018), because open field regions do not fractionate sulfur whereas close fields with resonant Alfvén waves do. In addition to this, in-situ measurements of abundances are less sensitive to interactions with local magnetic fields and plasma (Parenti et al. 2021).

The combination of HMI and EUV spectroscopy data can provide a more complete understanding of the dynamics and energetics of the solar atmosphere. The comparison of HMI magnetograms with EUV emission images can aid in associating magnetic structures to chromospheric and coronal features, such as flares, prominences, and coronal loops. By tracking the temporal and spatial evolution of these features, we can investigate the underlying physical mechanisms that govern the heating and acceleration of the plasma in the solar atmosphere.

Regarding temperature diagnostics, the results are to be taken with caution. First of all, the coronal assumption that is being made is a strong hypothesis and results in significant uncertainties in the results. Moreover, models for the CHIANTI database are still being improved, and it has been found that the formation temperature of transition region ions is probably overestimated in many cases. Strong lines in the EUV also present some anomalous ions (especially from Li-like and Na-like ions, in our case O VI and Ne VIII), which present additional uncertainties and a strong dependence on density. Single-line ratios accuracy and issues are discussed in details in Del Zanna et al. (2001) and Del Zanna & Mason (2003).

Another aspect that is still to be corrected is the PSF, and doing so will enable us to compute more precise and accurate Doppler maps (Plowman et al. 2022). This will provide additional information about sources of solar wind, as a significant portion of the slow solar wind would form in upflowing, blue-shifted plasma. The most promising aspect of these composition map analyses is the relative FIP bias maps, especially performed with the Linear Combination Ratio. Our maps show good consistency with previous publications, and will be the key for understanding the formation and source regions of the solar wind.

7. Conclusion

We present an overview of possible diagnostics techniques for analyzing SPICE composition observations, and more precisely for the connection mosaic performed in March 2022. Mapping the source regions on the surface of the Sun to the heliosphere using these connection mosaics are an important objective of Solar Orbiter and are planned to be performed periodically during future Solar Orbiter remote sensing windows.

From this preliminary mosaic, we have obtained encouraging results by reducing the data and extracting a range of quantities, and we explored the range of what SPICE data has to offer.

In addition to radiance maps, we have computed Differential Emission Measures, elemental abundances, and relative FIP bias maps from the SPICE data. This illustrates that SPICE has a wide array of outputs to provide and could be even more formidable if paired with *in-situ* analyses. Proposals for joint analysis have already been explored (Fludra & Landi 2018), and Solar Orbiter measurements are very promising for addressing the key questions of solar-terrestrial physics. Radiances inferred from this dataset show variances acceptable for active regions but quiet Sun discrepancies still need to be explained. More observations will complete the preliminary diagnostic performed in this work. The study of the radiance maps has shown that SPICE is able to capture complex solar structures with satisfying resolution (even with a factor-of-two binning in the slit direction for all maps). Isothermal temperatures (around $\log T = 5.8 / 5.9$) have been found for AR loop structures, with an enhancement of low-FIP elements of a factor 3-4. Structures in SPICE radiance maps can be easily associated with those in EUV observations which show excellent matching, allowing other SPICE quantities such as FIP bias to be oriented relative to those higher-resolution observations. After investigating three different methods of deriving FIP-bias maps it would seem that the LCR with NIII, NIV, SIV, SV works best (Fig 13) – showing high FIP values at the base of some AR structures, potentially the source of the Fast solar wind.

Expanding this analysis to include observations from other EUV instruments, such as Hinode/EIS will enable a broader temperature coverage, extending investigations to the higher corona.

Since this first composition mosaic has been released, a significant amount of progress has been made in the SPICE data pipeline (dark subtraction, WCS file correction, line choice) and modules are being developed (PSF correction, error computation). The next steps are to compute velocity maps inferred from SPICE data and compare the *in-situ* data with our results.

In the future, we will utilize combined measurements from SWA/HIS and Hinode/EIS to conduct comprehensive analyses of the data and validate the initial findings presented in this study. The inclusion of synoptic observations will further strengthen the database and minimize uncertainties associated with relying solely on a single dataset. These observations will not only provide comprehensive diagnostics from the chromosphere to the upper corona but also ensure temporal coverage of the specific regions under investigation.

In summary, SPICE offers a complete coverage of the transition region from chromospheric lines to coronal ones, complementing the observations and data from Hinode/EIS and SOHO/SUMER.

Acknowledgements. These efforts at SwRI for Solar Orbiter SPICE are supported by NASA under GSFC subcontract #80GSFC20C0053 to Southwest Research Institute. The development of the SPICE instrument has been funded by ESA member states and ESA (contract no. SOL.S.ASTR.CON. 00070). The work at GSFC is supported by NASZA funding for Solar Orbiter SPICE, and N. Zambrana-Prado is supported by cooperative agreement 80NSSC21M0180.

The German contribution to SPICE is funded by the Bundesministerium für Wirtschaft und Technologie through the Deutsches Zentrum für Luft und Raumfahrt e.V. (DLR), grants no. 50 OT 1001/1201/1901. The Swiss hardware contribution was funded through PRODEX by the Swiss Space Office (SSO). The UK hardware contribution was funded by the UK Space Agency. S.L.Yardley would like to thank STFC via the consolidated grant (STFC ST/V000497/1). G. Del Zanna acknowledges support from STFC (UK) via the consolidated grant to the atomic astrophysics group at DAMTP, University of Cambridge (ST/T000481/1). Python modules used for this work include `numpy`, `matplotlib`, `astropy`, `sunpy`, `scipy`, `spice_uncertainties` available at https://git.ias.u-psud.fr/spice/spice_uncertainties/-/tree/main, `EMToolKit` available at <https://github.com/jeplozman/EMToolKit> and `cblind` available at <https://github.com/volodia99/cblind>. The author would like to particularly thank N. Zambrana-Prado, G. Del Zanna and H. E. Mason for their help writing this paper.

References

- Abbo, L., Ofman, L., Antiochos, S. K., et al. 2016, *Space Sci. Rev.*, 201, 55
 Andretta, V. & Del Zanna, G. 2014, *A&A*, 563, A26
 Antonucci, E., Romoli, M., Andretta, V., et al. 2020, *A&A*, 642, A10
 Asplund, M., Amarsi, A. M., & Grevesse, N. 2021, *A&A*, 653, A141
 Astropy Collaboration, Robitaille, T. P., Tollerud, E. J., et al. 2013, *A&A*, 558, A33
 Baker, D., Brooks, D. H., Démoulin, P., et al. 2015, *The Astrophysical Journal*, 802, 104
 Baker, D., van Driel-Gesztelyi, L., Brooks, D. H., et al. 2019, *ApJ*, 875, 35
 Berger, T., De Pontieu, B., Fletcher, L., et al. 1999, *Solar Physics*, 190
 Berghmans, D., Antolin, P., Auchère, F., et al. 2023, First Perihelion of EUV on the Solar Orbiter mission, arXiv:2301.05616 [astro-ph, physics:physics]
 Borovsky, J. E. 2020, *Journal of Atmospheric and Solar-Terrestrial Physics*, 204, 105271
 Brooks, D. H., Janvier, M., Baker, D., et al. 2022, *ApJ*, 940, 66
 Brown, J. C., Dwivedi, B. N., Sweet, P. A., & Almléaky, Y. M. 1991, *A&A*, 249, 277
 Cranmer, S. R., Gibson, S. E., & Riley, P. 2017, *Space Sci. Rev.*, 212, 1345
 Cranmer, S. R., van Ballegoijen, A. A., & Edgar, R. J. 2007, *ApJS*, 171, 520
 Del Zanna, G., Bromage, B. J. I., Landi, E., & Landini, M. 2001, *A&A*, 379, 708
 Del Zanna, G., Landini, M., & Mason, H. E. 2002, *A&A*, 385, 968
 Del Zanna, G. & Mason, H. E. 2003, *A&A*, 406, 1089
 Dufresne, R. P., Del Zanna, G., & Mason, H. E. 2023, *MNRAS*, 521, 4696
 Earl, N., Tollerud, E., Jones, C., et al. 2022, *astropy/specutils: V1.7.0*
 Feldman, U., Warren, H. P., Brown, C. M., & Doschek, G. A. 2009, *The Astrophysical Journal*, 695, 36
 Fludra, A., Caldwell, M., Giunta, A., et al. 2021, *Astronomy & Astrophysics*, 656, A38
 Fludra, A. & Landi, E. 2018, in *Space Weather of the Heliosphere: Processes and Forecasts*, ed. C. Foullon & O. E. Malandraki, Vol. 335, 87–89
 G., D. & H.E., M. 2018, *Living Reviews in Solar Physics*, 15
 Gallagher, P. T., Moon, Y.-J., & Wang, H. 2002, *Solar Physics*, 209, 171
 García Marínodríguez, C., Pacros, A., Strandmo, S., et al. 2021, *A&A*, 646, A121
 Guennou, C., Auchère, F., Soubrié, E., Bocchialini, K., & Parenti, S. 2012a, *The Astrophysical Journal Supplement Series*, 203, 26, arXiv:1210.2302 [astro-ph]
 Guennou, C., Auchère, F., Soubrié, E., et al. 2012b, *The Astrophysical Journal Supplement Series*, 203, 25
 Hassler, D. M., Dammasch, I. E., Lemaire, P., et al. 1999, *Science*, 283, 810
 Horbury, T. S., O'Brien, H., Carrasco Blazquez, I., et al. 2020, *A&A*, 642, A9
 Howard, R. A., Vourlidis, A., Colaninno, R. C., et al. 2020, *A&A*, 642, A13
 Judge, P. G., Hubeny, V., & Brown, J. C. 1997, *ApJ*, 475, 275
 Krieger, A. S., Timothy, A. F., & Roelof, E. C. 1973, *Sol. Phys.*, 29, 505
 Krucker, S., Hurford, G. J., Grimm, O., et al. 2020, *A&A*, 642, A15
 Maksimovic, M., Bale, S. D., Chust, T., et al. 2020, *A&A*, 642, A12
 Mohan, A., Landi, E., & Dwivedi, B. N. 2000, *A&A*, 364, 835
 Müller, D., Marsden, R. G., St. Cyr, O. C., & Gilbert, H. R. 2013, *Sol. Phys.*, 285, 25
 Müller, D., St. Cyr, O. C., Zouganelis, I., et al. 2020, *A&A*, 642, A1
 Owen, C. J., Bruno, R., Livi, S., et al. 2020a, *A&A*, 642, A16
 Owen, C. J., Bruno, R., Livi, S., et al. 2020b, *A&A*
 Parenti, S., Chifu, I., Del Zanna, G., et al. 2021, *Space Sci. Rev.*, 217, 78
 Plowman, J. & Caspi, A. 2020, *The Astrophysical Journal*, 905, 17
 Plowman, J. E., Auchère, F., Cuadrado, R. A., et al. 2022, *SPICE PSF Correction: General Framework and Capability Demonstration*
 Raymond, J. C. & Doyle, J. G. 1981, *ApJ*, 245, 1141
 Reames, D. V. 2018, *Sol. Phys.*, 293, 47
 Robitaille, T., Ginsburg, A., Mumford, S., et al. 2023, *astropy/reproject: v0.10.0*
 Rochus, P., Auchère, F., Berghmans, D., et al. 2020, *A&A*, 642, A8

- Rodríguez-Pacheco, J., Wimmer-Schweingruber, R. F., Mason, G. M., et al. 2020, *A&A*, 642, A7
- Rouillard, A. P., Pinto, R. F., Vourlidas, A., et al. 2020, *A&A*, 642, A2
- Schmelz, J. T., Reames, D. V., von Steiger, R., & Basu, S. 2012, *ApJ*, 755, 33
- Solanki, S. K., del Toro Iniesta, J. C., Woch, J., et al. 2020, *Astronomy & Astrophysics*, 642, A11
- SPICE Consortium, Anderson, M., Appourchaux, T., et al. 2020, *A&A*, 642, A14
- Strong, K. T. 1980, Phd thesis, University College London
- Warren, H. P., Brooks, D. H., Doschek, G. A., & Feldman, U. 2016, *ApJ*, 824, 56
- Warren, H. P., Brooks, D. H., Doschek, G. A., & Feldman, U. 2016, *The Astrophysical Journal*, 824, 56
- Widing, K. G. & Feldman, U. 1989, *ApJ*, 344, 1046
- Widing, K. G. & Feldman, U. 2001, *The Astrophysical Journal*, 555, 426
- Winkler, W. 1976, *Acta Astronautica*, 3, 435
- Zambrana Prado, N. & Buchlin, E. 2019, *Astronomy & Astrophysics*, 632, A20
- Zambrana Prado, N., Buchlin, E., Kucera, T., Young, P., & SPICE team. in prep.
- Zouganelis, I., De Groof, A., Walsh, A. P., et al. 2020, *A&A*, 642, A3

Appendix A: Line fitting and comments on the windows

In order to properly analyze the spectrum (intensity, shift, turbulence), a fit is needed. We rely on the `specutils` (Earl et al. 2022) module from the Astropy Collaboration et al. (2013). We have chosen to model the spectrum with a sum Gaussian curves and a constant to fit both the peaks and the continuum. We require an initial guess for each of the parameters of the Gaussian (here, the mean μ , the standard deviation σ and the amplitude A). The guesses are made using the `astropy estimate_line_parameters`, which relies on a least-squares fit to the input data. If more than one peak is fitted, we divide the spectrum in sub-spectra to compute those initial guesses, as indicated in Table 1. Once the parameters for each Gaussian are obtained, we compute the final fit using all the whole spectrum. The results of the single-peak fit are presented in Fig. A.1.

The main source of noise in SPICE files is shot noise, also called Poisson noise, which tends to dominate at lower photon counts. The model of errors that will be used in the following analysis is the sum (the noise is additive) of the errors induced by the dark (Poissonian), background (Poissonian), read (Gaussian) and line (Poissonian) noises. For each pixel, these noise sources add in quadrature, as

$$N_{total} = \sqrt{N_{dark}^2 + N_{background}^2 + N_{read}^2 + N_{line}^2} \quad (\text{A.1})$$

A noise floor is also initialized based on SPICE's uncertainty package, developed by E. Buchlin. Its value is equal to the sum of dark current and background signal levels.

The goodness of fit is computed as the residuals between the model predictions and the observed data points. For this non-linear least squares fitting, the goal is to minimize the sum of squares of these residuals. The goodness of fit is evaluated as the mean of the difference between the observed data points and the corresponding values predicted by the model, sliced with the same windows we use for estimating the Gaussian parameters. This goodness of fit can be negligible in regard to the instrumental error (especially for lines N IV and O VI, which are single-peaked).

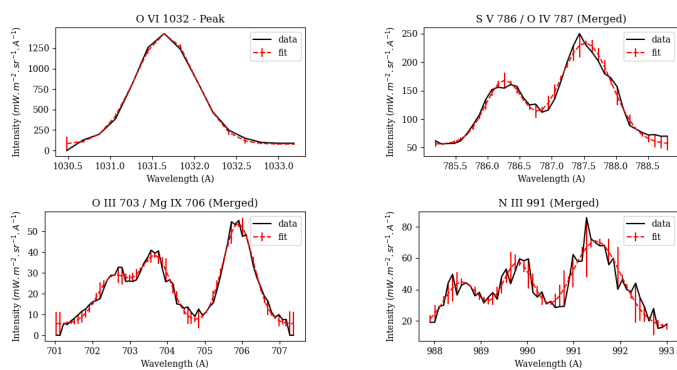


Fig. A.1: Examples of fits for single, double and triple Gaussian models over the active region 12958.

A.1. O III 703 / Mg IX 706

This window raises an additional challenge because of the O III multiplet around 703 Å. Indeed, within the range [702.3 - 703.8], there are 6 O III lines and two non-negligible S III lines. This

multiplicity of lines makes the fitting much more difficult, because one fitted peak will not correspond to a single ion. That is why the O III results should be taken with great caution, as we do not know exactly the contribution of each line. In order to have greater accuracy and more reliable results, we chose (despite a higher computing time) to fit a model involving three Gaussians, even though each Gaussian will fit a blend of several ions. We focused on two main oxygen lines (O III 702.8 – highly blended with S III 702.7 / 702.8 and O III 703.8) and the Mg IX 706 line.

As all blended windows, the contribution of the strongest line is often non-negligible when doing a line fitting, even though two peaks are clearly distinguishable. If one wanted to be more exact with the continuum fitting, instead of modeling it by a constant, one could model a linear function for the magnesium emission peak, which is tilted because of the contribution of the strong O III line.

A.2. Ne VIII 770 / Mg VIII 772

The same problem as mentioned above is encountered with this window, in addition to the fact that the magnesium VIII is barely detectable outside of very bright and hot active regions. As seen on Figure A.2, the quiet Sun measurements of Mg VIII can not be reliable; however, within an active region, we have sufficient signal, even though it stays fairly weak.

A.3. S IV 748 / S IV 750

As can be seen on Figure A.2, the spectra of this window looks less reliable than others, what with looks like a bad dark subtraction coupled with very wide peaks. The asymmetry on the second peak above 750 Å is very likely due to a blend with the Mg IX 749.5 Å. This might result in an over-estimation of the sulfur line in the diagnostics – it can be seen on Figure C.2 that AR structures are brighter in the S IV 750 Å line.

A.4. N III 991

The N III window raises the same concern as the O III / Mg IX window. We also chose a model with 3 Gaussians to maximize our accuracy. We focused on the peak at 988.6 Å, which may be a blend of O I and Na VI, the peak at 989.8 Å accounting for N III and the N III 991.5 Å peak. See Figure A.1 for an example of the fits. An issue that we encountered was the presence of cosmic rays, which the fitting algorithm frequently misidentified as emission peaks. To address this issue, we imposed constraints on the standard deviation during the generation of the Gaussian model. While this measure did not entirely resolve the problem, it successfully eliminated the majority of cosmic rays.

The maps obtained are shown in Figures C.1 and C.2. The windows Ne VIII / Mg VIII, N IV - Peak and O VI - Peak present a binning on the spectral axis, which required a multiplication of the radiances by a factor of two.

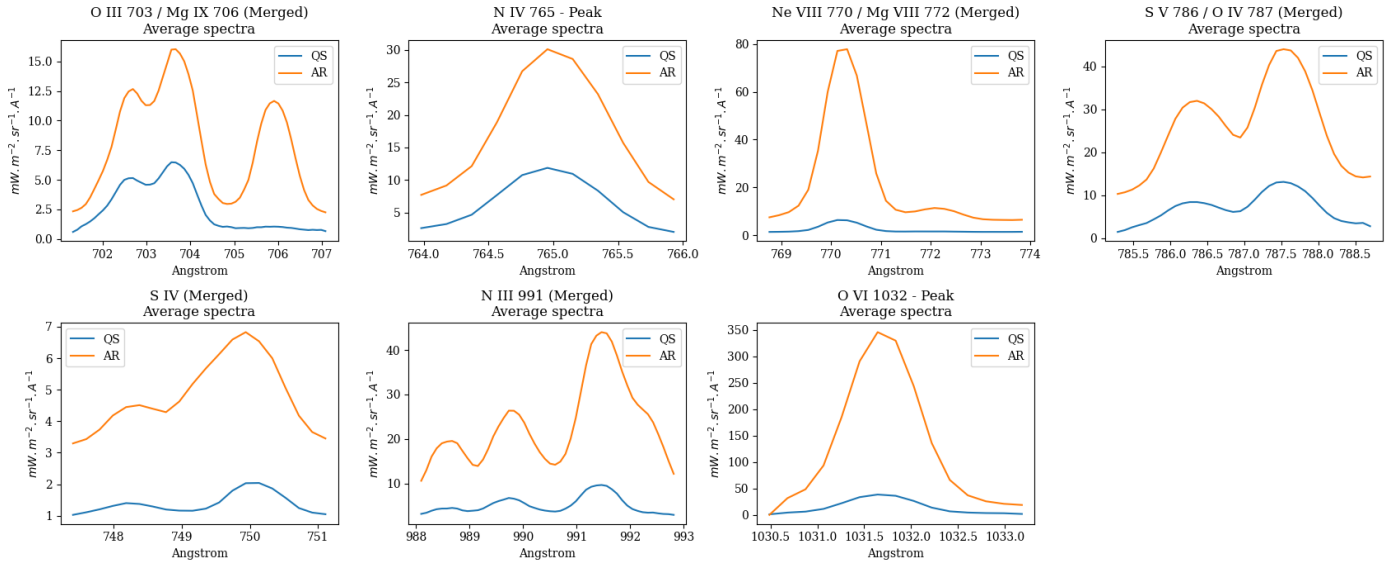


Fig. A.2: Averaged spectra over the cubes of the top file of the mosaic. The blue curve represents the spectra averaged over a QS area, the orange one the spectra averaged over an AR area. The AR and QS areas correspond to S1 and S2, respectively, on Figure 3.

Appendix B: Contribution functions

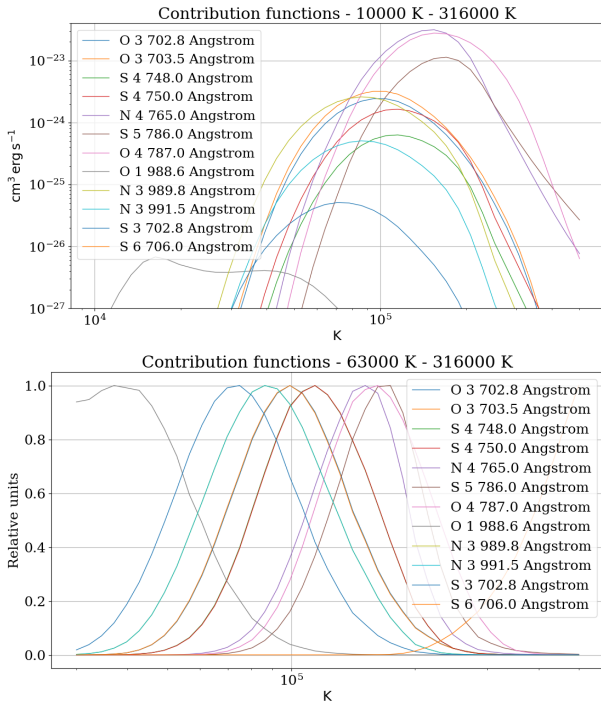


Fig. B.1: Contribution functions for lower temperature lines - 6.3×10^4 - 3.16×10^5 K. Top: contribution functions displayed on a log-log scale. Bottom: contribution functions normalized and displayed on a linear y-scale.

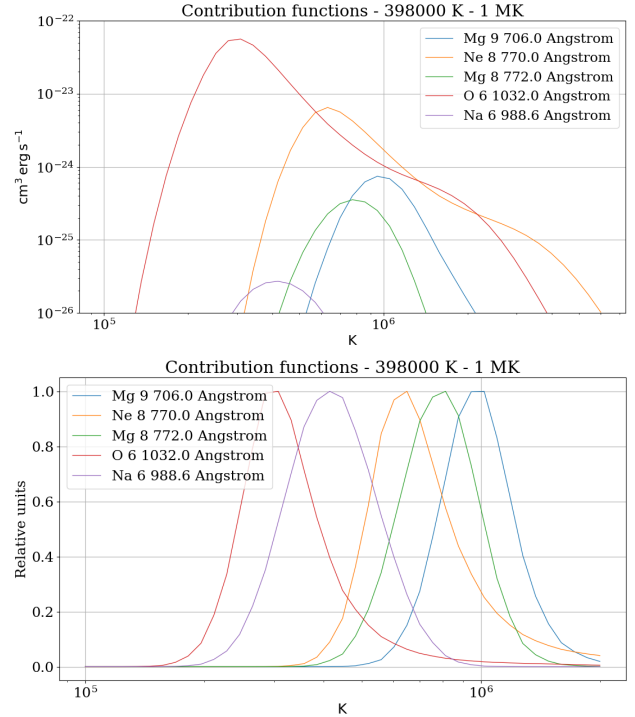


Fig. B.2: Contribution functions for higher temperature lines - 3.9×10^5 - 1.0×10^6 K. Right and left panels are the same as Figure B.1.

As can be seen on figures B.1 and B.2, where contribution functions C_{ij} are plotted with an electron density of $n_e = 2 \times 10^{-9}$ cm^{-3} , only a few couples of lines satisfy the condition of having "close enough" contribution functions. Among those, the best pairs would be S V / O IV, S V / N IV, S IV / O III and undoubtedly S IV 748 / S IV 750. For higher temperatures, the contribution functions are more sparse. However, the couples Mg IX /

Ne VIII, Mg VIII / Ne VIII and Mg IX / Mg VIII would still be usable.

Appendix C: Radiance maps

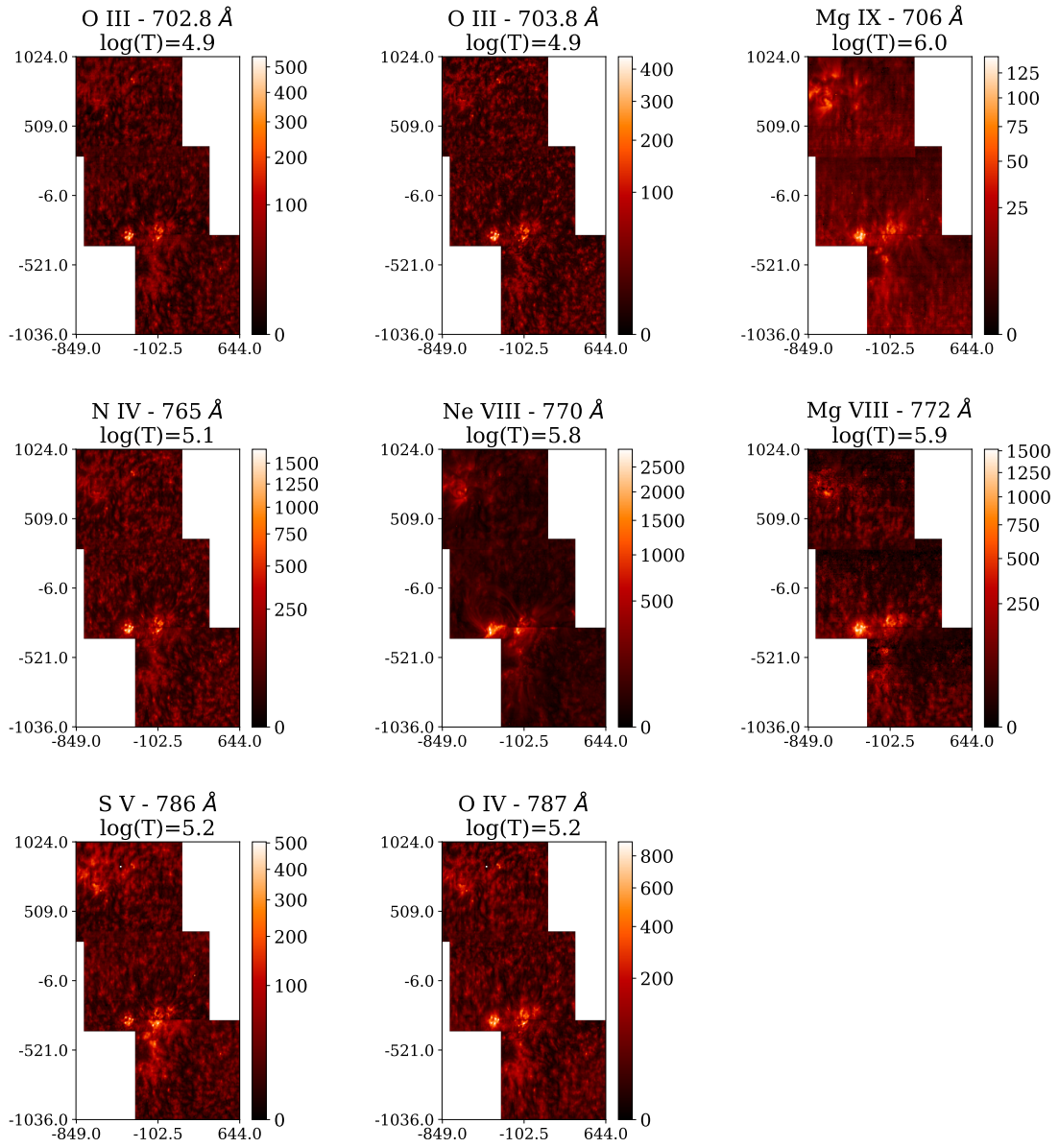


Fig. C.1: Radiances maps from the lines recorded by SPICE during the SOOP Mosaic on March 2nd, 2022 (Seven first lines). Units are in $\text{mW sr}^{-1} \text{m}^{-2}$.

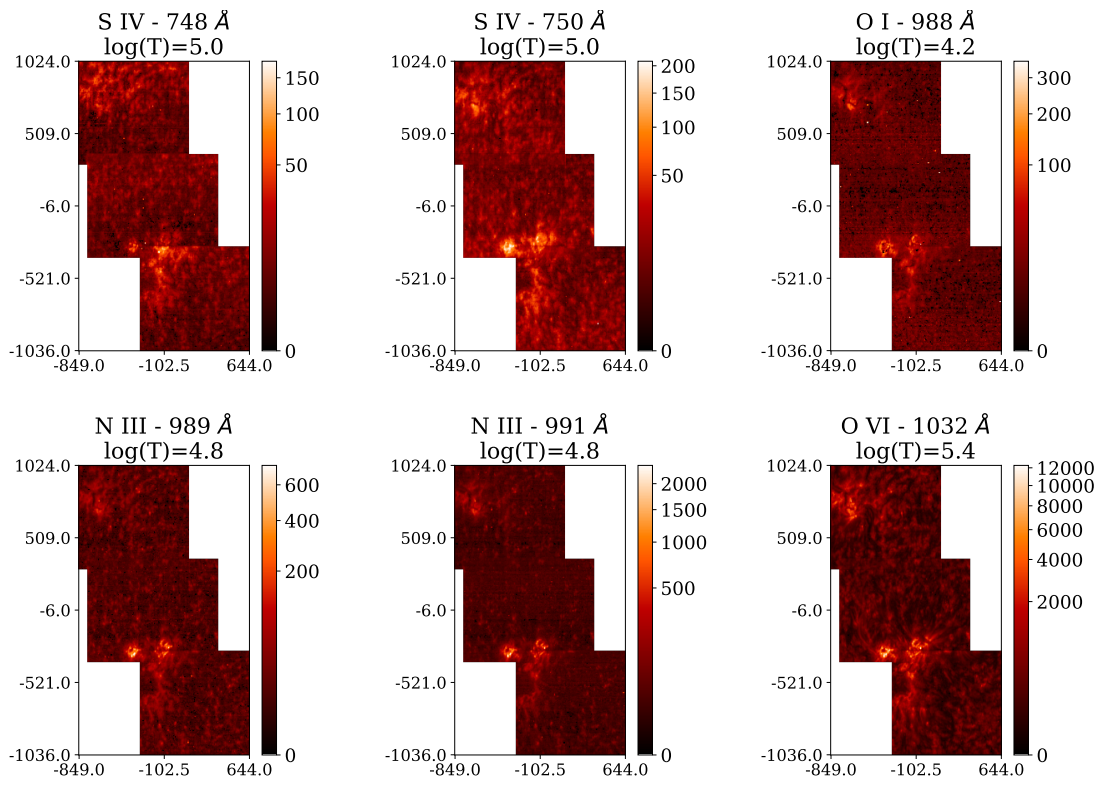


Fig. C.2: Radiance maps from the lines recorded by SPICE during the SOOP Mosaic on March 2nd, 2022. Same units as in Figure C.1.